


# High-resolution Navier-Stokes simulations of Richtmyer-Meshkov instability with reshock

Man Long Wong <sup>\*</sup>

*Department of Aeronautics and Astronautics, Stanford University, Stanford, California 94305, USA*

Daniel Livescu<sup>†</sup>

*CCS-2, Los Alamos National Laboratory, Los Alamos, New Mexico 87545, USA*

Sanjiva K. Lele<sup>‡</sup>

*Department of Aeronautics and Astronautics and Department of Mechanical Engineering, Stanford University, Stanford, California 94305, USA*



(Received 5 December 2018; published 25 October 2019)

The interaction of a Mach-1.45 shock wave with a perturbed planar interface between sulfur hexafluoride and air is studied through high-resolution two-dimensional (2D) and three-dimensional (3D) shock-capturing adaptive mesh refinement simulations of multispecies Navier-Stokes equations. The sensitivities of time-dependent statistics on grid resolution for 2D and 3D simulations are evaluated to ensure the accuracy of the results. The numerical results are used to examine the differences between the development of 2D and 3D Richtmyer-Meshkov instability during two different stages: (1) initial growth of hydrodynamic instability from multimode perturbations after first shock and (2) transition to chaotic or turbulent state after reshock. The effects of the Reynolds number on the mixing in 3D simulations are also studied through varying the transport coefficients.

DOI: [10.1103/PhysRevFluids.4.104609](https://doi.org/10.1103/PhysRevFluids.4.104609)

## I. INTRODUCTION

Richtmyer-Meshkov (RM) instability, or RMI [1,2], is a fundamental hydrodynamic flow instability that occurs when a shock wave passes through a material interface between fluids of different densities. The instability is initiated by the deposition of vorticity at the interface due to the misalignment in the pressure and density gradients across the shock wave and material interface. Studying RMI is very important for understanding the dynamics of supernovae and other astrophysical explosions, mixing enhancement in supersonic and hypersonic combustion, and turbulence and mixing limitations for inertial confinement fusion [3–5].

The study of RMI through physical experiments is challenging because the flows are transient, the initial conditions of the interface are difficult to characterize, and uncertainty-quantified measurements are hard to obtain. The initial perturbation grows nonlinearly soon after the passage of the shock through the interface. The growth of the mixing region is known to be largely dependent on the characteristics of initial perturbation [6–13] and hence a precise control of the initial conditions is required from experiments. If the Reynolds number is sufficiently high, small-scale turbulent features will develop beyond the mixing transition. Characterizing the turbulent

---

<sup>\*</sup>wongml@stanford.edu

<sup>†</sup>livescu@lanl.gov

<sup>‡</sup>lele@stanford.edu

mixing requires high-resolution temporal and spatial measurements of both the density and velocity fields. The simultaneous planar laser-induced fluorescence (PLIF) and particle image velocimetry (PIV) measurements have been used to collect density and velocity data from shock-induced mixing problems in many previous studies [13–17]. However, the method is only limited to the measurements of the fields in a two-dimensional plane and data of other important quantities such as pressure and temperature are still out of reach. As a consequence, numerical simulations are commonly used as a complement to study the turbulent mixing induced by RMI.

As this moment, direct numerical simulation (DNS) of turbulent mixing from RMI is still computationally too expensive. However, many high-fidelity simulations and large eddy simulations (LES's) have been conducted in the past to study the development of turbulent mixing from RMI. Thornber *et al.* [6] showed the strong influence on the growth of instability from perturbations with different bandwidths using shock-capturing simulations. Hill *et al.* [18] performed LES's of RMI with reshock using a hybrid shock-capturing and bandwidth-optimized center-difference scheme with stretched-vortex subgrid-scale model in an adaptive mesh refinement framework and their results showed good agreement with experimental data. Lombardini *et al.* [19] later used the same numerical method to examine the Atwood number dependence of RMI, followed by a Mach number dependence study [20]. The uncertainty of turbulence statistics in under-resolved simulations of RMI was later explored by Tritschler *et al.* [21] for different numerical methods. While all studies mentioned above focused on the baroclinic instability in planar geometry, there are also some studies of the instabilities with inclined [22] and spherical [23,24] interfaces.

Although typical applications of shock-driven turbulent mixing require the multicomponent governing equations to be solved in three-dimensional (3D) domains, one may still desire to conduct two-dimensional (2D) simulations to characterize the dynamics in the nonlinear preturbulent regime and take advantage of the lower requirement on computational resources. Before the onset of fully developed turbulence and especially during the initial growth of the shock-induced instability, there may be similarities in the development of the instability between 2D and 3D configurations. Olson and Greenough [25] compared the 2D and 3D simulations of RMI using the artificial fluid LES method but the mixing statistics obtained from their highest resolution simulations are still very grid sensitive. Thornber and Zhou [26] also studied the 2D RMI with up to 64 realizations of inviscid simulations to reduce the statistical variability of their results but they did not study the effect of reshock on the 2D instability. In this paper, we have conducted a large number of realizations of high-resolution Navier-Stokes simulations of 2D RMI with reshock to investigate the difference between 2D and 3D RMI-induced mixing.

In many previous RMI studies [6,7,10,11], the hydrodynamic equations were solved without the molecular viscous and diffusive terms. The argument for not including these terms is that the physical dissipation or diffusion can be represented by numerical dissipation or diffusion, by assuming that there is only forward cascade of energy from large-scale to small-scale features [27,28]. While this might be relevant during the decay of the fully turbulent mixing region, the molecular transport terms could have a strong effect on the initial growth of mixing layer before mixing transition occurs. In this work, we have chosen the initial conditions for the 3D simulations such that the flows inside the mixing layers have not transitioned to turbulence yet before reshock. By varying the transport coefficients, multiple cases with effectively different turbulent Reynolds numbers have been conducted to study the diffusive and viscous effects on the shock-driven mixing before and after reshock.

## II. GOVERNING EQUATIONS

The equations solved in this study are the conservative multicomponent Navier-Stokes equations:

$$\frac{\partial \rho Y_i}{\partial t} + \nabla \cdot (\rho \mathbf{u} Y_i) = -\nabla \cdot \mathbf{J}_i, \quad (1)$$

$$\frac{\partial \rho \mathbf{u}}{\partial t} + \nabla \cdot (\rho \mathbf{u} \mathbf{u} + p \delta) = \nabla \cdot \boldsymbol{\tau}, \quad (2)$$

$$\frac{\partial E}{\partial t} + \nabla \cdot [(E + p)\mathbf{u}] = \nabla \cdot (\boldsymbol{\tau} \cdot \mathbf{u} - \mathbf{q}_c - \mathbf{q}_d), \quad (3)$$

where  $\rho$ ,  $\mathbf{u} = [u, v, w]^T = [u_1, u_2, u_3]^T$ ,  $p$ , and  $E$  are the density, velocity vector, pressure, and total energy per unit volume of the fluid mixture, respectively.  $Y_i$  is the mass fraction of species  $i \in [1, 2, \dots, N]$ , with  $N$  being the total number of species. All  $Y_i$ 's sum up to one by definition.  $\mathbf{J}_i$  is diffusive mass flux for species  $i$ .  $\boldsymbol{\tau}$ ,  $\mathbf{q}_c$ , and  $\mathbf{q}_d$  are viscous stress tensor, conductive heat flux, and interspecies diffusional enthalpy flux, respectively.  $\delta$  is the identity tensor.

The mixture is assumed to be ideal and calorically perfect, with

$$E = \rho \left( e + \frac{1}{2} \mathbf{u} \cdot \mathbf{u} \right), \quad (4)$$

$$p = (\gamma - 1) \rho e, \quad e = c_v T, \quad (5)$$

where  $e$  and  $T$  are respectively specific internal energy and temperature of the mixture.  $\gamma$  and  $c_v$  are the ratio of specific heats and specific heat at constant volume of the mixture.

The multicomponent diffusive mass flux of species  $i$  is given by Hirschfelder *et al.* [29]:

$$\mathbf{J}_i = \rho \frac{M_i}{M^2} \sum_{j=1}^N M_j \tilde{D}_{ij} \nabla X_j, \quad (6)$$

where  $M_i$  and  $X_i$  are respectively the molecular weight and molar fraction of species  $i$ .  $M$  is the molecular weight of the mixture and  $\tilde{D}_{ij}$  is the  $m$ th element of the matrix of ordinary multicomponent diffusion coefficients  $\tilde{\mathbf{D}}$ . The molar fraction of species  $i$  is given by

$$X_i = \frac{M}{M_i} Y_i. \quad (7)$$

Barodiffusion is neglected in this study since the shock Mach number is relatively small [30] and after the passage of the shock the flow is close to incompressible (see below). The multicomponent diffusive mass flux is reduced to the Fick's law for binary mixture:

$$\mathbf{J}_i = -\rho D_i \nabla Y_i, \quad i = 1, 2, \quad (8)$$

where  $D_1 = D_2$  is the binary diffusion coefficient.

The viscous stress tensor  $\boldsymbol{\tau}$  for a Newtonian mixture is

$$\boldsymbol{\tau} = 2\mu \mathbf{S} + \left( \mu_v - \frac{2}{3}\mu \right) \delta (\nabla \cdot \mathbf{u}), \quad (9)$$

where  $\mu$  and  $\mu_v$  are the shear viscosity and bulk viscosity respectively of the mixture.  $\mathbf{S}$  is the strain-rate tensor given by

$$\mathbf{S} = \frac{1}{2} [\nabla \mathbf{u} + (\nabla \mathbf{u})^T]. \quad (10)$$

The conductive flux and the interspecies diffusional enthalpy flux [31] are given by

$$\mathbf{q}_c = -\kappa \nabla T, \quad (11)$$

$$\mathbf{q}_d = \sum_{i=1}^N h_i \mathbf{J}_i, \quad (12)$$

where  $\kappa$  is the thermal conductivity of the mixture.  $h_i$  is the specific enthalpy of species  $i$ :

$$h_i = c_{p,i} T, \quad (13)$$

where  $c_{p,i}$  is the specific heat at constant volume of species  $i$ .

TABLE I. Initial conditions of the postshock state and the preshock states of the light- and heavy-fluid sides.

Quantity	Postshock SF <sub>6</sub>	Preshock SF <sub>6</sub>	Air
$\rho$ (kg m <sup>-3</sup> )	11.97082	5.972866	1.145601
$p$ (Pa)	218005.4	101325.0	101325.0
$T$ (K)	319.9084	298.0	298.0
$u$ (m s <sup>-1</sup> )	98.93441	0.0	0.0

The equations and mixing rules for the fluid properties  $\gamma$ ,  $c_v$ ,  $c_{p,i}$ ,  $\mu$ ,  $\mu_v$ ,  $\kappa$ , and  $D_i$  are given in Appendixes F and G.

### III. NUMERICAL METHODS

Simulations were performed using the in-house Hydrodynamics Adaptive Mesh Refinement Simulator (HAMeRS). The parallelization of the code and all the construction, management, and storage of cells are facilitated by the Structured Adaptive Mesh Refinement Application Infrastructure (SAMRAI) library [32–36] from Lawrence Livermore National Laboratory (LLNL). The explicit form of sixth-order localized dissipation weighted compact nonlinear scheme (WCNS) [37], which is designed to add sufficient dissipation around shocks and regions with large gradients for numerical stability and minimum dissipation in smooth regions to capture vortical features, is used for the hyperbolic part of the governing equations. Explicit sixth-order finite differences are used to compute the derivatives of diffusive and viscous fluxes in nonconservative form. A third-order total variation diminishing Runge-Kutta (RK-TVD) scheme [38] is adopted for time integration. Various sensors are employed to identify regions of interest for adaptive mesh refinement (AMR). These include gradient sensor on pressure field and wavelet sensor [39] on density field to detect shock waves and mixing regions, respectively. An additional sensor based on mass fractions is also used to assist the detection of mixing regions. Further details on the numerical methods and the sensors for mesh refinement are given in Appendixes D and E, respectively.

### IV. NUMERICAL SETUP

In our 2D numerical setup, the height of the domain in the transverse direction is chosen to be 2.5 cm. To facilitate the comparison between 2D and 3D results in later sections, the 3D numerical setup is chosen to be the extension of the 2D setup with a transverse sectional area of 2.5 cm  $\times$  2.5 cm. In both 2D and 3D simulations, a shock wave with Mach number  $Ma = 1.45$  is launched initially in a sulfur hexafluoride (SF<sub>6</sub>) region and interacts with a diffuse material interface between ideal gases SF<sub>6</sub> and air. The computational domain and initial conditions for the 3D simulations are shown in Fig. 1(b). Boundaries are periodic in the transverse directions and reflective boundary conditions are applied at the end wall. The length of the numerical shock tube is chosen to be large enough (50 cm) such that no features leave the domain at the open-sided boundary during the simulations. The 2D configuration [Fig. 1(a)] is basically a cross-sectional view of the 3D setup.

The preshocked conditions correspond to  $T = 298$  K and  $p = 101325$  Pa. The fluids are initially at rest in the simulation reference frame. Table I shows the initial conditions in different portions of the domain. The initial Atwood number,  $At = (\rho_{\text{SF}_6} - \rho_{\text{air}})/(\rho_{\text{SF}_6} + \rho_{\text{air}})$ , across the interface is 0.68. The density, pressure, temperature, and Mach number relations across the initial shock in SF<sub>6</sub> in the shock reference frame are given by the Rankine-Hugoniot jump

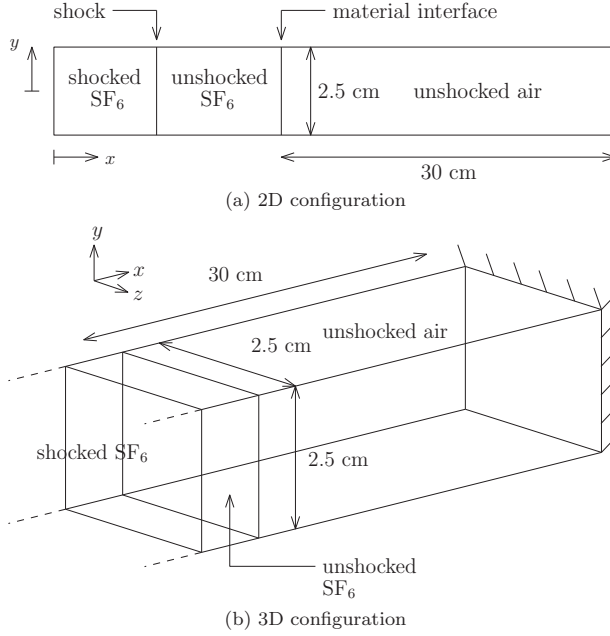


FIG. 1. Schematic diagrams of initial flow fields and computational domains for the 2D (a) and 3D (b) simulations.

conditions:

$$\frac{\rho'}{\rho} = \frac{\left(\frac{\gamma_{\text{SF}_6} + 1}{2}\right) \text{Ma}^2}{1 + \left(\frac{\gamma_{\text{SF}_6} - 1}{2}\right) \text{Ma}^2}, \quad (14)$$

$$\frac{p'}{p} = \frac{\frac{2\gamma_{\text{SF}_6}}{\gamma_{\text{SF}_6} - 1} \text{Ma}^2 - 1}{\frac{\gamma_{\text{SF}_6} + 1}{\gamma_{\text{SF}_6} - 1}}, \quad (15)$$

$$\frac{T'}{T} = \left( \frac{\gamma_{\text{SF}_6} \text{Ma}^2 - \left(\frac{\gamma_{\text{SF}_6} - 1}{2}\right)}{\frac{\gamma_{\text{SF}_6} + 1}{2}} \right) \left( \frac{1 + \left(\frac{\gamma_{\text{SF}_6} - 1}{2}\right) \text{Ma}^2}{\left(\frac{\gamma_{\text{SF}_6} + 1}{2}\right) \text{Ma}^2} \right), \quad (16)$$

$$\text{Ma}'^2 = \left( \frac{1 + \left(\frac{\gamma_{\text{SF}_6} - 1}{2}\right) \text{Ma}^2}{\gamma_{\text{SF}_6} \text{Ma}^2 - \left(\frac{\gamma_{\text{SF}_6} - 1}{2}\right)} \right), \quad (17)$$

where quantities without primes are preshock quantities and those with primes are postshock quantities.

Figure 2 shows the space-time ( $x-t$ ) diagram for different features in a one-dimensional (1D) flow representation.  $t = 0$  is set as the instance of the first arrival of the shock at the interface. The initial position of the incident shock is chosen such that the first shock-interface interaction occurs at 0.05 ms after the start of simulation. Since the shock traverses the interface from the heavy fluid side, a shock is transmitted to the light fluid side and a rarefaction wave is reflected back to the heavy fluid side. The shock wave also accelerates the interface toward the end wall. After hitting the end wall, the shock is reflected back and interacts with the interface again at  $t \approx 1.15$  ms. Since the reflected shock passes from the light fluid side during the reshock of interface, a transmitted shock and a reflected shock are generated. The reflected shock will eventually lead to a second

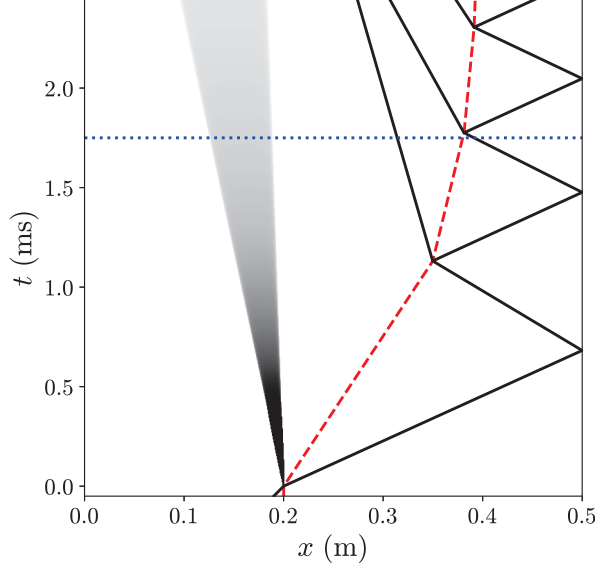


FIG. 2.  $x$ - $t$  diagram showing the propagation of material interface, shock waves, and rarefaction. Red dashed line, material interface; black lines, shock waves; gray region, rarefaction. The blue dotted line indicates the end time of all simulations.

reshock. The simulations are stopped at  $t = 1.75$  ms, which is the time just before second reshock, as the grid resolution requirements become too large to accurately capture this flow stage.

In order to trigger the flow instability, perturbations are seeded on the material interfaces. Multimode perturbations for 2D and 3D simulations are given by the following two equations:

$$S(y) = A \sum_m \cos\left(\frac{2\pi m}{L_y}y + \phi_m\right), \quad (18)$$

$$S(y, z) = A \sum_m \cos\left(\frac{2\pi m}{L_y}y + \phi_m\right) \cos\left(\frac{2\pi m}{L_{yz}}z + \psi_m\right), \quad (19)$$

where  $L_y = L_{yz} = 2.5$  cm. In both 2D and 3D simulations, there are 11 perturbation modes with wave number  $m$  between 20 and 30 in each transverse direction. Constant amplitude  $A = \sqrt{2} \times 0.01$  mm is used for each mode and random phase shifts  $\phi_m$  and  $\psi_m$  between 0 and  $2\pi$  are added to each mode to prevent adding up of harmonics. The perturbation for the 3D case is a combination of “egg-crate” modes, which are mode forms commonly used to model perturbations created by wire meshes in experiments [40–42]. However, instead of using a single mode, we have chosen a narrow band of “egg-crate” modes with different phases to account for possible variation in wire mesh spacing in a physical experiment and to facilitate symmetry breaking. Another approach commonly used in previous studies [10,18,21] to break symmetry is to superpose a small random perturbation on a single dominant “egg-crate” mode. Note that all 3D simulations presented in this work have the exact perturbation with same set of relative phases.

A finite thickness is prescribed for the initial interface between  $\text{SF}_6$  and air. The partial density of each gas,  $\rho Y_i$ , is smoothed across the material interface initially with the following formulation:

$$f_{sm} = \frac{1}{2} \left[ 1 + \operatorname{erf} \left( \frac{x - L_i - S}{\epsilon_i} \right) \right], \quad (20)$$

$$(\rho Y_i)_{sm} = (\rho Y_i)_L (1 - f_{sm}) + (\rho Y_i)_R f_{sm}, \quad (21)$$

where  $L_i$  is the initial location of the material interface.  $\epsilon_i$  is the characteristic thickness of the initial material interface and is set to 1 mm. Therefore, the initial thickness has the same order of magnitude as the wavelengths of the perturbation modes. In the RMI simulations by Lombardini *et al.* [20] and Tritschler *et al.* [21], the initial interface thicknesses are also comparable to the wavelengths of the dominant perturbation modes. Note that the relatively large initial diffuse interface thickness will lower the early time growth rate compared to the sharp interface case [43,44], but the study of this effect is not the focus of this work.

To reduce the statistical variability associated with the very few modes present at the 1D interface, all statistical results for the 2D simulations are obtained by ensemble averaging over 24 realizations with different random phase shifts  $\phi_m$  in the initial perturbations. We have found that 24 realizations are sufficient for the statistical convergence of quantities of interests. The details are discussed in Appendix A.

## V. CHARACTERISTIC SCALES OF TWO-DIMENSIONAL AND THREE-DIMENSIONAL PROBLEMS

In this section, the characteristic length scales, timescales, and growth rates of the 2D and 3D problems are determined from the initial conditions and the linear theory.

The growth rate  $\dot{\eta}_{\text{imp}}^{2D}$  for a 2D small single-mode perturbation with initial amplitude  $\eta_0^{2D}$  from an impulsive acceleration on a discontinuous interface obtained from linear theory by Richtmyer [1] is given by

$$\dot{\eta}_{\text{imp}}^{2D} = \frac{2\pi}{\lambda^{2D}} U_i A t \eta_0^{2D}, \quad (22)$$

where  $\lambda^{2D}$  is the wavelength of the perturbation and  $U_i$  is the change in interface velocity induced by the incident shock wave. It can be extended to the growth rate of a 3D single-mode interface as

$$\dot{\eta}_{\text{imp}}^{3D} = \sqrt{2} \frac{2\pi}{\lambda^{3D}} U_i A t \eta_0^{3D}, \quad (23)$$

where  $\lambda^{3D} = \lambda_y^{3D} = \lambda_z^{3D}$  is the wavelength of the perturbation in either  $y$  or  $z$  directions.

Although material interfaces are smoothed initially in the numerical setup, the growth rates from linear theory still become relevant after the initial diffusive growth, as the initial characteristic thicknesses of all cases in this work are the same. In this work, the equivalent single-mode amplitudes  $\eta_0^{2D}$  and  $\eta_0^{3D}$  are estimated as the standard deviations of the initial perturbations.

The equivalent single-mode wavelengths,  $\lambda^{2D}$  and  $\lambda^{3D}$ , can be estimated from the integral length scales. Since the initial perturbations are periodic with only few modes, the integral length scales are computed from the energy spectra of the perturbations, instead of the autocorrelations. This is necessary, as the autocorrelation of a periodic signal is itself periodic and does not approach zero when based on only few modes, no matter how large the computational domain is. The integral length scales for the 2D and 3D cases,  $l^{2D}$  and  $l^{3D}$ , are computed as

$$l^{2D}/l^{3D} = \frac{2\pi}{\int_0^\infty E(k) dk} \int_0^\infty \frac{E(k)}{k} dk, \quad (24)$$

where  $E(k)$  is the energy spectrum of the perturbation that depends on angular wave number  $k$ . Note that  $E(k)$  is the radial energy spectrum in the  $yz$  plane and  $k$  is the radial angular wave number for the 3D case. The wavelengths  $\lambda^{2D}$  and  $\lambda^{3D}$  are then estimated as

$$\lambda^{2D} = l^{2D}, \quad \lambda^{3D} = \sqrt{2} l^{3D}. \quad (25)$$

The characteristic timescales can be obtained from the impulsive growth rates as

$$\tau^{2D} = \frac{\lambda^{2D}}{\dot{\eta}_{\text{imp}}^{2D}}, \quad \tau^{3D} = \frac{\lambda^{3D}}{\dot{\eta}_{\text{imp}}^{3D}}. \quad (26)$$

TABLE II. Initial characteristic scales for the 2D and 3D cases.

Case	$\eta_0$ (mm)	$\lambda$ (mm)	$\dot{\eta}_{\text{imp}}$ (m s <sup>-1</sup> )	$\tau$ (ms)
2D	0.0331	1.02	18.4	0.0552
3D	0.0234	1.02	18.4	0.0551

Table II shows the standard deviations, wavelengths, growth rates from impulsive theory, and characteristic timescales from the initial conditions of the 2D and 3D cases. It can be seen from the table that the growth rates and characteristic timescales for both 2D and 3D cases are virtually identical with the initial conditions chosen.  $\eta_0$  values for both cases are smaller than 5% of the corresponding  $\lambda$  value. Therefore, it is expected that the perturbations grow linearly after first shock. Note that in many previous simulations, including those by Lombardini *et al.* [20] and Tritschler *et al.* [21], the initial amplitudes of the perturbations are more than 10% of the wavelengths and hence the perturbations are already in the nonlinear regime initially.

A method that can take the mode compression and coupling effects into account to estimate initial growth rates was proposed by Weber *et al.* [45]. The 2D and 3D growth rates for discontinuous interfaces estimated with the corresponding method are, respectively, 10.3 and 10.0 m s<sup>-1</sup>. The 2D and 3D initial growth rates measured from the mixing widths (defined in Sec. VI) computed from the simulations are 0.86 and 0.82 m s<sup>-1</sup>, respectively. The essentially identical initial growth rates for the 2D and 3D problems estimated with different methods show that the 2D and 3D initial conditions are designed appropriately for fair comparison between the two problems. The growth rates measured from the simulation results are much smaller than the ones given by the impulsive theory or method by Weber *et al.* [45] for discontinuous interfaces due to the large initial diffuse interface thicknesses. For simplicity, we have chosen the impulsive growth rates given by Eqs. (22) and (23) as the characteristic growth rates to normalize physical quantities in this work.

## VI. GRID SENSITIVITY ANALYSIS

To understand the sensitivities of numerical results to the grid spacing, a grid sensitivity study is conducted for both 2D and 3D problems. Tables III and IV show the grids used in the grid sensitivity analysis. In all grid settings, there are three levels of meshes in total, with two levels of mesh refinement. The refinement ratios in each direction are respectively 1:2 and 1:4 from base level to second level and from second level to the finest level. For the 2D problem, the base grids have number of grid points in the transverse direction varying from 128 points (grid D) to 1024 points (grid G). The highest resolution grid has grid spacing of 3.05  $\mu\text{m}$  at the finest level, and 24 realizations are conducted on each grid to reduce the statistical variability of the data. As for the 3D problem, the base grids have a number of grid points in the transverse directions varying from 32 points (grid B) to 128 points (grid D). The highest resolution grid has grid spacing of 24.4  $\mu\text{m}$  at the finest level. Figure 3 shows the visualizations of the mixing layer with the shock waves and the AMR grid for the 3D problem just before reshock and at the end of simulation after reshock with grid D settings.

TABLE III. Different grids used for the 2D problem. Three levels of grids, with 1:8 overall refinement ratio in each direction, are used in all cases.

Grid	Base grid resolution	Refinement ratios	Finest grid spacing ( $\mu\text{m}$ )
D	2560 $\times$ 128	1:2, 1:4	24.4
E	5120 $\times$ 256	1:2, 1:4	12.2
F	10240 $\times$ 512	1:2, 1:4	6.10
G	20480 $\times$ 1024	1:2, 1:4	3.05



TABLE IV. Different grids used for the 3D problem. Three levels of grids with 1:8 overall refinement ratio in each direction are used in all cases.

Grid	Base grid resolution	Refinement ratios	Finest grid spacing ( $\mu\text{m}$ )
B	$640 \times 32 \times 32$	1:2, 1:4	97.7
C	$1280 \times 64 \times 64$	1:2, 1:4	48.8
D	$2560 \times 128 \times 128$	1:2, 1:4	24.4

The grid sensitivities of different statistical quantities are examined through comparison of their temporal evolution corresponding to different grids. The quantities analyzed include the mixing width  $W$ , mixedness  $\Theta$ , integrated turbulent kinetic energy (TKE), integrated scalar dissipation rate  $\chi$ , and integrated enstrophy  $\Omega$ . The mixing width and mixedness are defined as

$$W = \int 4\bar{X}_{\text{SF}_6}(1 - \bar{X}_{\text{SF}_6})dx, \quad (27)$$

$$\Theta = \frac{\int \overline{X_{\text{SF}_6}(1 - X_{\text{SF}_6})} dx}{\int \bar{X}_{\text{SF}_6}(1 - \bar{X}_{\text{SF}_6})dx}, \quad (28)$$

where  $\bar{\cdot}$  is the mean of the respective quantity in the homogeneous directions (y direction for 2D and yz plane for 3D). The mean is also computed using an additional averaging over the 24 realizations (ensemble averaging) for the 2D case.

The mathematical formulations for TKE, scalar dissipation rate, and enstrophy are given by

$$\text{TKE} = \frac{1}{2}\rho u''_i u''_i, \quad (29)$$

$$\chi = D_{\text{SF}_6} \nabla Y_{\text{SF}_6} \cdot \nabla Y_{\text{SF}_6}, \quad (30)$$

$$\Omega = \rho \boldsymbol{\omega} \cdot \boldsymbol{\omega}, \quad (31)$$

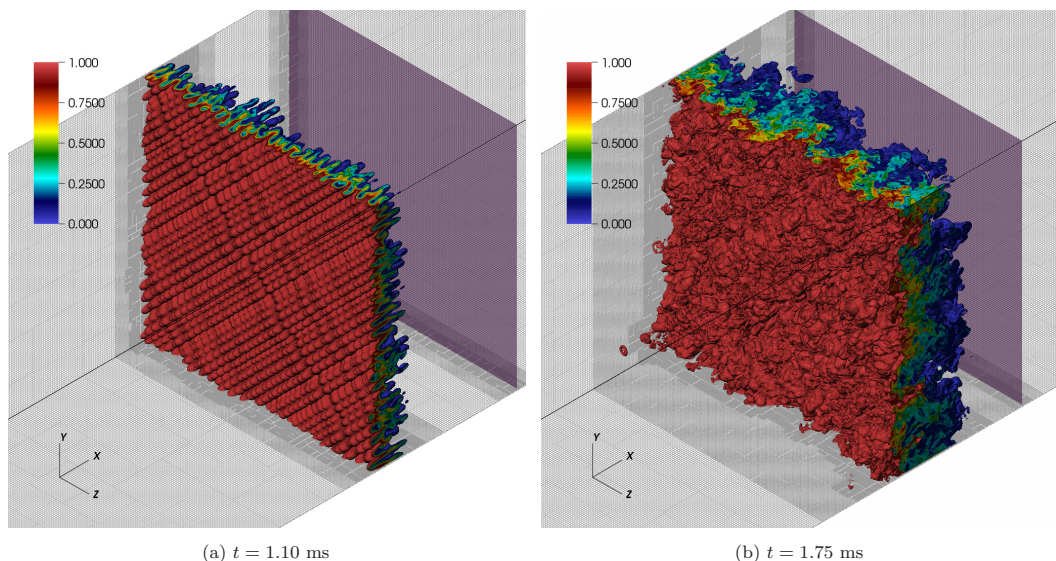


FIG. 3. Isovolumes of the  $\text{SF}_6$  mole fraction and  $X_{\text{SF}_6}$ , at different times for the 3D problem with grid D. The color bars indicate the value of  $X_{\text{SF}_6}$ . The transparent magenta planes represent the locations of shocks. The AMR grid hierarchy is shown on the side walls of the domain. (a)  $t = 1.10$  ms. (b)  $t = 1.75$  ms.

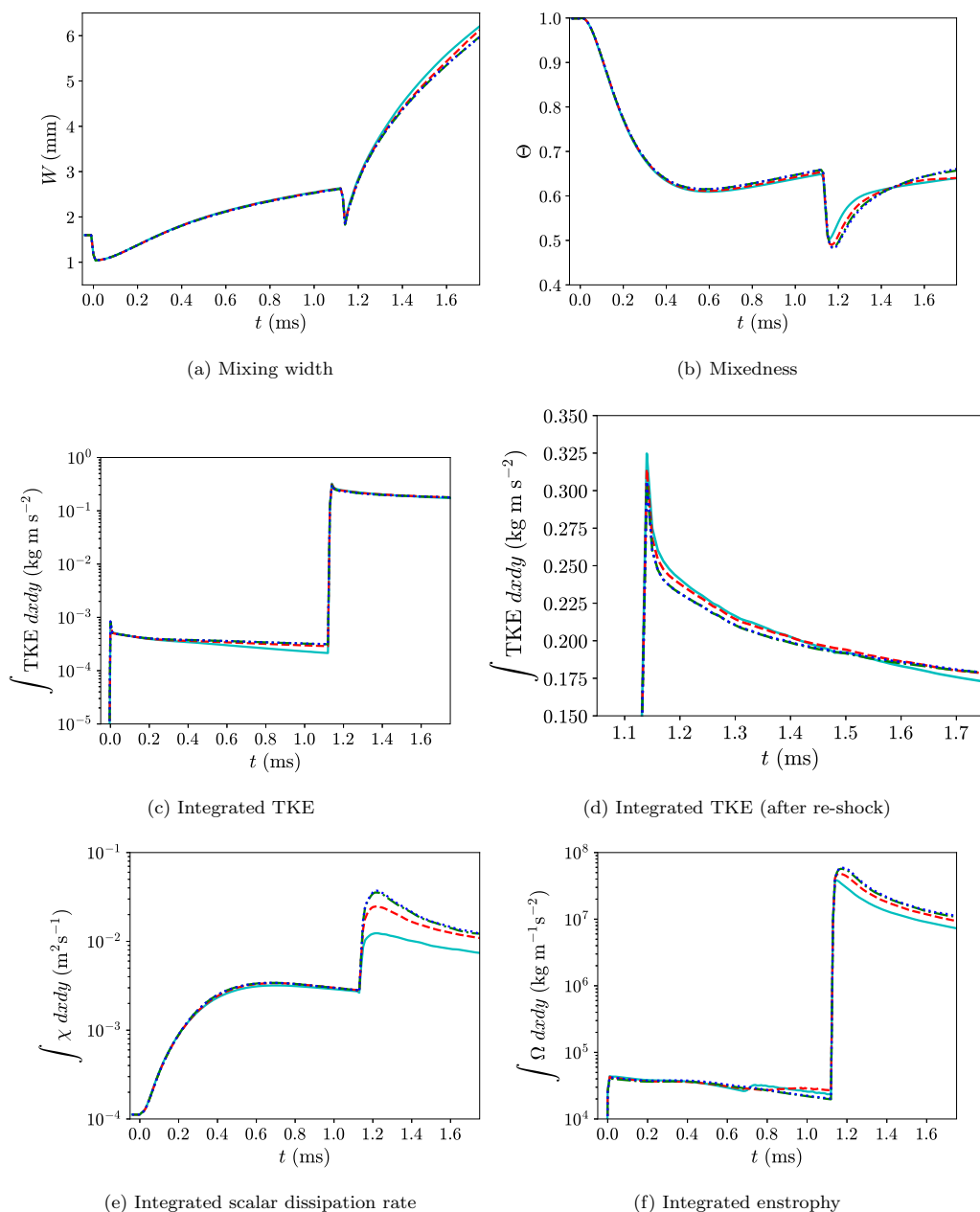


FIG. 4. Grid sensitivities of different statistical quantities over time for the 2D problem. Cyan solid line, grid D; red dashed line, grid E; green dash-dotted line, grid F; blue dotted line, grid G.

where  $u_i'' = u_i - \tilde{u}_i$  and  $\boldsymbol{\omega} = \nabla \cdot \mathbf{u}$  is the vorticity. The Favre (density-weighted) mean of the velocity is defined by  $\tilde{u}_i = \overline{\rho u_i} / \bar{\rho}$ . The integrated quantities are calculated over the full domain.

Figures 4 and 5 show the time evolution of various statistical quantities computed on different grids for the 2D and 3D cases, respectively. The mixing width defines the large-scale characteristic

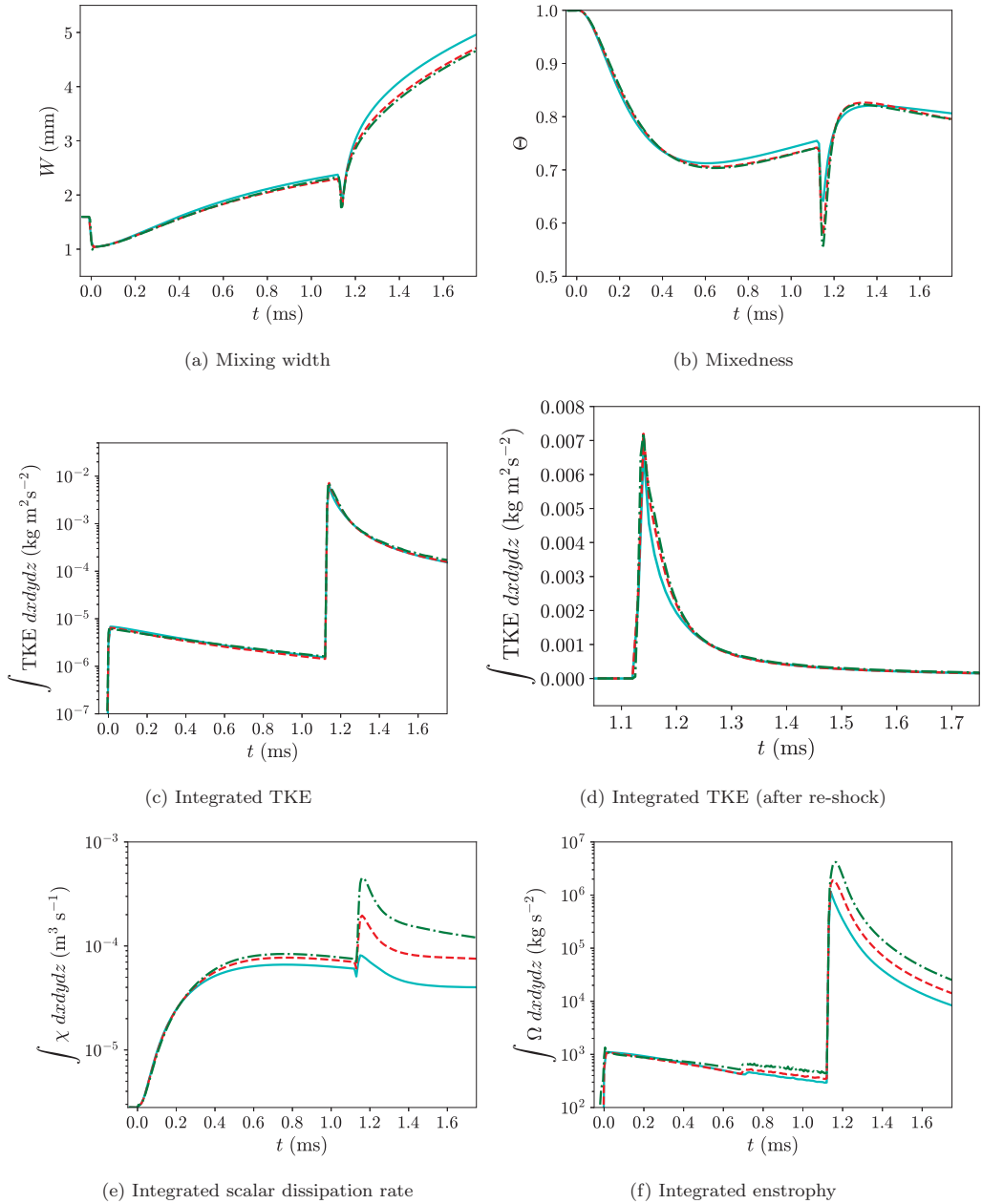


FIG. 5. Grid sensitivities of different statistical quantities over time for the 3D problem. Cyan solid line, grid B; red dashed line, grid C; green dash-dotted line, grid D.

length of the mixing layer. The growth of this quantity is largely dominated by the entrainment of the fluids through convective motions. The mixedness is commonly used as an estimation of the amount of fluids that is molecularly mixed within the mixing layer [16,17,20,21,46]. It is generally interpreted as the ratio of the amount of fluids molecularly mixed to the amount of fluids entrained by convection. By comparing the results obtained on grids F and G from Fig. 4, it can be seen that

both mixing width and mixedness for the 2D case are fully grid converged. Similarly, for the 3D case, it can be seen from Fig. 5 that the grid also has very little effect on the mixing width and mixedness at the highest grid resolution level (grid D).

In the flow problem being studied, kinetic energy is deposited at the material interface when the shock passes through the interface and TKE is generated subsequently. TKE is largely dominated by the low-wave-number eddies or large-scale features. After the passage of the shock, TKE decays as it is converted to internal energy through viscous dissipation. Grid convergence of the domain-integrated TKE is obtained at the highest resolutions considered for both 2D and 3D problems, as seen in Figs. 4 and 5.

While mixing width and TKE are dominated by large-scale features, scalar dissipation rate and enstrophy are mainly associated with high-wave-number features closer to Batchelor and Kolmogorov scales. Tritschler *et al.* [21] noticed that peaks of the scalar dissipation rate and enstrophy spectra shift to higher wave numbers and magnitudes when smaller scales are resolved with finer grid in the grid sensitivity analysis of their RMI simulations. Therefore, the grid convergence requirements for these two quantities are expected to be stricter than mixing width and TKE. From Fig. 4, we can see that grid convergence for both domain-integrated scalar dissipation rate and enstrophy is still achieved for the 2D problem, but only at the finest grid. For the 3D problem, grid convergence of both integrated quantities is only obtained for a short duration after first shock (until  $t \approx 0.25$  ms) with the finest grid. Since the quantities that depend on high-wave-number features are not grid converged for the 3D case, the simulations performed are still far from DNS level, especially immediately after reshock. Moreover, we estimate that the incident and transmitted shock thicknesses are at  $O(10)$  and  $O(1)$  microns respectively. Even with the ultrahigh grid resolution setting (grid G) for the 2D case, it is believed that the transmitted shock is still far from well resolved and the solutions around the shock are regularized by the shock-capturing scheme.

An assumption of implicit LES (ILES) is that one may use a numerically dissipative scheme as a substitute for an explicit subgrid scale (SGS) model, i.e., assuming that the numerical scheme has the same dissipative effects as subgrid scales have on the resolved scales [27,28]. While the present simulations do not use an explicit SGS model and thus share this aspect of ILES, we do not assume that the numerical scheme used provides a good model for the SGS effects in the flows we study. We recognize that SGS effects in variable-density flows are subjects of active recent studies [22,47,48] and require further research using DNS and experimental data. We also stress that the regularization effects or truncation errors of the scheme used in the present work were *not* designed to model the SGS effects. Therefore, in order to examine the numerical effects on the turbulence statistics, an extensive grid convergence analysis is provided in this section to show that most statistics of interest discussed in later sections are reasonably captured by the 3D simulations.

## VII. SETUP FOR THREE-DIMENSIONAL SIMULATIONS WITH REDUCED REYNOLDS NUMBERS

In order to study the effect of the Reynolds number on the development of 3D RMI, the 3D problem presented in the previous sections is repeated with the same initial conditions and the grid D settings, but with increased transport coefficients for each species ( $D_i$ ,  $\mu_i$ ,  $\mu_{v,i}$ , and  $\kappa_i$ ). The transport coefficients are increased in the simulations by artificially multiplying the values computed using physical models given in Appendix F with constant factors. Two cases, with transport coefficients increased by factors of 2 and 4, are simulated.

Figure 6 shows the time evolution of the means of the Reynolds numbers based on the mixing width,  $W$ , and mean integral length scale of SF<sub>6</sub> mole fraction,  $\langle l_{x_{\text{SF}_6}} \rangle$ , ( $\langle \text{Re}_W \rangle$  and  $\langle \text{Re}_l \rangle$ ), Schmidt number ( $\langle \text{Sc} \rangle$ ), and Prandtl number ( $\langle \text{Pr} \rangle$ ). The mean denoted by  $\langle \cdot \rangle$  corresponds to an additional

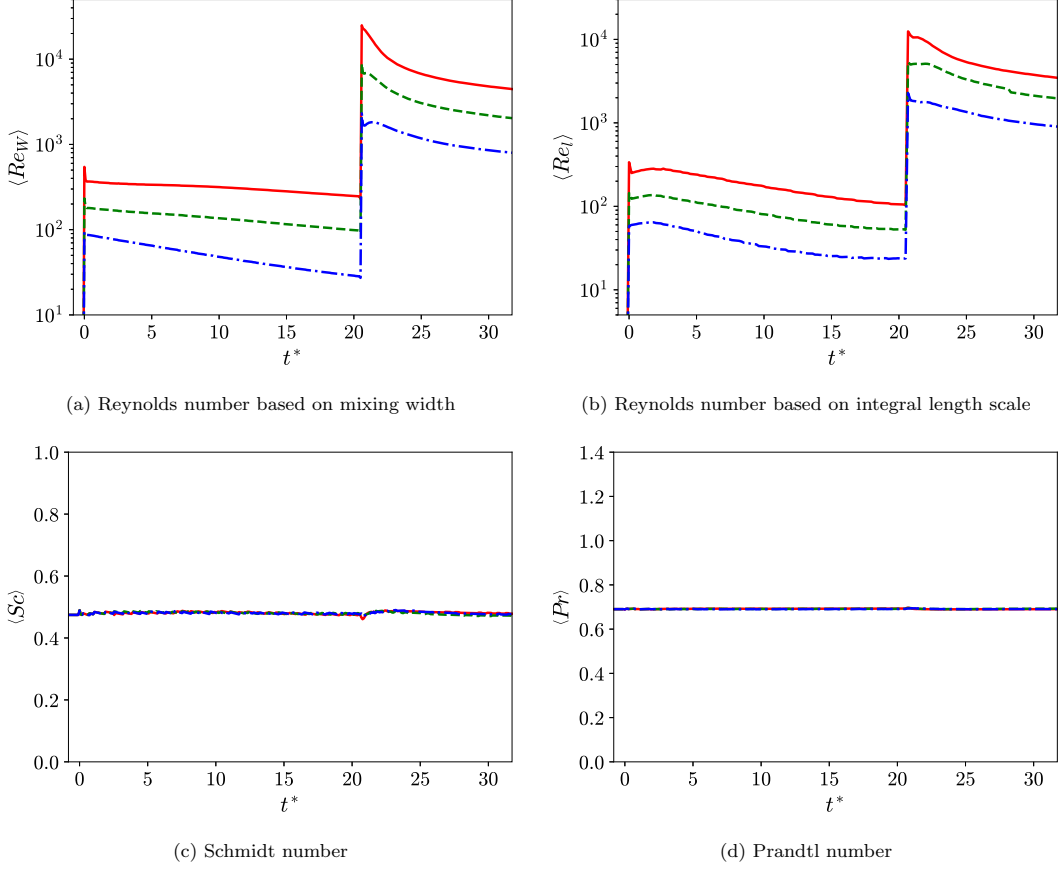


FIG. 6. Comparison of the time evolution of different dimensionless numbers between the 3D cases with different transport coefficients. Red solid line, physical transport coefficients; green dashed line,  $2\times$  physical transport coefficients; blue dash-dotted line,  $4\times$  physical transport coefficients.

averaging over the central part of the mixing layer of the quantities computed over the lines or planes.  $Re_W$ ,  $Re_l$ ,  $Sc$ , and  $Pr$  are defined as

$$Re_W = \frac{\bar{\rho} u_{\text{rms}} W}{\bar{\mu}}, \quad (32)$$

$$Re_l = \frac{\bar{\rho} u_{\text{rms}} \langle l_{X_{\text{SF}_6}} \rangle}{\bar{\mu}}, \quad (33)$$

$$Sc = \frac{\bar{\mu}}{\bar{\rho} \bar{D}_{\text{SF}_6}}, \quad (34)$$

$$Pr = \frac{\bar{c}_p \bar{\mu}}{\bar{k}}, \quad (35)$$

where  $u_{\text{rms}} = \sqrt{u_i' u_i'' / 3}$ . The central part of the mixing layer is defined as the regions where cross-sectional planes satisfy

$$4\bar{X}_{\text{SF}_6} (1 - \bar{X}_{\text{SF}_6}) \geq 0.9. \quad (36)$$

The nondimensional time,  $t^*$ , is defined by

$$t^* = \frac{t}{\tau_c}, \quad (37)$$

where  $\tau_c = \tau^{3D}$ . Figure 6 shows that increasing the transport coefficients mostly affects the Reynolds numbers, while other nondimensional quantities such as Schmidt and Prandtl numbers within the central part of mixing layer remain almost unchanged over time. The Reynolds number values are close when calculated based on the mixing width or integral length scale since these length scales have similar orders of magnitude. The simulations with reduced Reynolds numbers are further discussed in the next section.

### VIII. COMPARISON AND ANALYSIS OF TWO-DIMENSIONAL AND THREE-DIMENSIONAL CASES

This section contains the main results of the paper. First, the levels of compressibility and non-Boussinesq effects are assessed using the turbulent Mach number and an effective Atwood number. Then, some features of the mixing are discussed using the mean and variance profiles of the mole fraction as well as its probability density function. This is then followed by a discussion of the turbulent kinetic energy and the anisotropy of Reynolds normal stresses. Finally, the time evolution of the spectra of the mole fraction and energy defined based on the momentum with density-weighted fluctuation of the velocity after reshock is examined. All results for the 2D case in this section are obtained by ensemble averaging over 24 realizations computed with grid G, while those for the 3D cases are obtained with grid D. It is found that 24 realizations are sufficient to achieve statistical convergence for most of the quantities of interest for the 2D case in this work (as discussed in Appendix A).

#### A. Flow compressibility and effective Atwood number

Several aspects of compressibility of a flow can be measured from the turbulent Mach number,  $Ma_t$ , which is defined as

$$Ma_t = \frac{\sqrt{u'_i u'_i}}{\bar{c}}, \quad (38)$$

where  $c = \sqrt{\gamma p / \rho}$  is the speed of sound.

Figure 7 shows the time evolution of turbulent Mach number within the central part of the mixing layer for the 2D and 3D cases with different transport coefficients. The turbulent Mach number is very close to zero for all cases before reshock. After reshock, the turbulent Mach number for all 3D cases decays quickly to zero asymptotically after a jump. The turbulent Mach number for the 2D case is larger than that for the 3D cases because velocity fluctuations remain larger in the 2D case after reshock. This is further discussed in Sec. VIII F. Overall though, all simulations are only weakly compressible as  $\langle Ma_t \rangle$  for each case is always smaller than 0.3.

Another measure of the compressibility effects is the magnitudes of thermodynamic fluctuations. From the ideal equation of state, the mixture density,  $\rho$ , depends on pressure,  $p$ , mixture molecular weight,  $M$ , and temperature,  $T$ , through  $\rho = pM/(R_u T)$ . Figure 8 shows the normalized covariances of  $\rho$  with  $p$ ,  $M$ , and  $1/T$  across the normalized position  $x^*$  just after first shock and reshock from the 2D and 3D simulations with physical transport coefficients. The normalized position is defined as

$$x^*(x, t) = \frac{x - x_i(t)}{W(t)}, \quad (39)$$

where  $x_i$  is the location of the interface from the  $x$ - $t$  diagram (Fig. 2). It is shown in Fig. 8 that, for both cases, the covariance of the mixture density and mixture molecular weight is the largest among

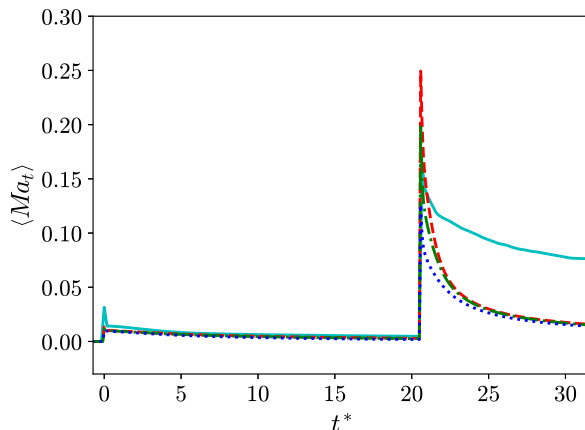


FIG. 7. Comparison of the time evolution of means of turbulent Mach number,  $\langle Ma_t \rangle$ , in the central part of mixing layer between the 2D and 3D problems. Cyan solid line, 2D with physical transport coefficients; red dashed line, 3D with physical transport coefficients; green dash-dotted line, 3D with  $2\times$  physical transport coefficients; blue dotted line, 3D with  $4\times$  physical transport coefficients.

the three covariances at the two times just after impulsive accelerations considered. Compared to this covariance, the covariance of the mixture density and reciprocal of temperature is much smaller and that of the mixture density and pressure is virtually zero, which means the mixing layer is very weakly compressible.

As a consequence of the nearly incompressible flow behavior, from the ideal equation of state, density mainly depends on the composition of the flow through the mixture molecular weight,  $M$ , as the quantity  $\rho R_u/M = p/T$ , is quasiuniform across the mixing regions, where  $R_u$  is the universal gas constant. The quasiuniform behavior of the ratio  $p/T$  is further discussed in Appendix B. Note that if  $p/T$  is uniform in the flow, the variable-density Navier-Stokes equations can be derived as the infinite speed of sound limit of the fully compressible Navier-Stokes equations with multispecies transport [30]. Further, if the ratio  $p/T$  is strictly uniform, one can also easily derive a linear

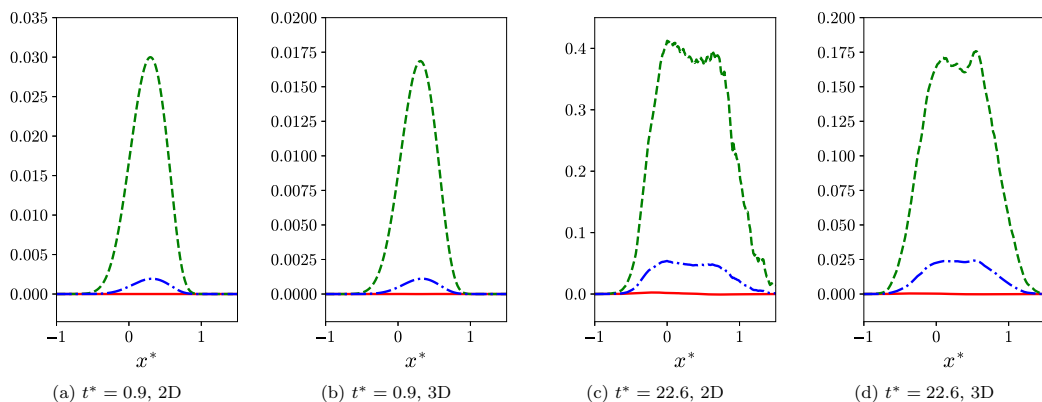


FIG. 8. Profiles of normalized covariances of mixture density with other quantities just after first shock ( $t^* = 0.9$ ) and just after reshock ( $t^* = 22.6$ ) for the 2D and 3D problems with physical transport coefficients. Red solid line,  $\overline{\rho' p'} / (\overline{\rho} \overline{p})$ ; green dashed line,  $\overline{\rho' M'} / (\overline{\rho} \overline{M})$ ; blue dash-dotted line,  $\overline{\rho' (1/T')} / (\overline{\rho} \overline{(1/T)})$ .

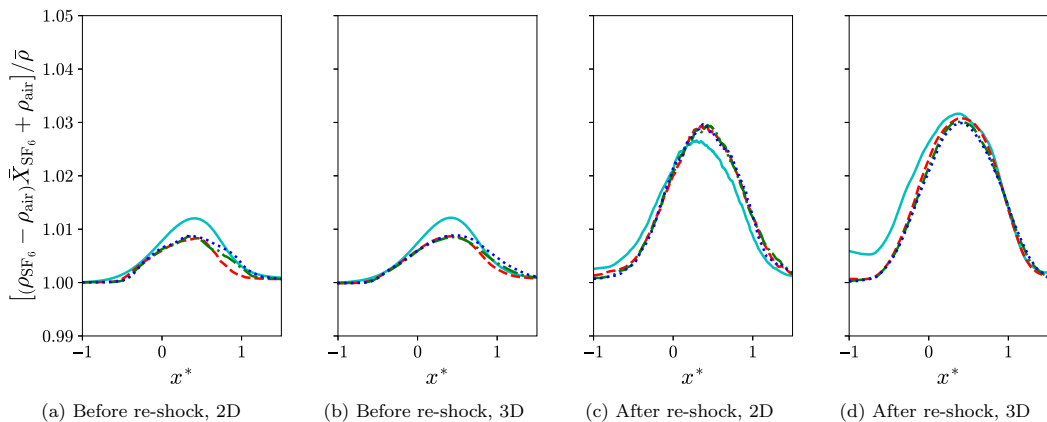


FIG. 9. Profiles of the ratio between the reconstructed density using the incompressible assumption and true density at different times for the 2D and 3D problems with physical transport coefficients. Before reshock:  $t^* = 0.9$  (cyan solid line);  $t^* = 7.5$  (red dashed line);  $t^* = 14.1$  (green dash-dotted line);  $t^* = 20.7$  (blue dotted line). After reshock:  $t^* = 22.6$  (cyan solid line);  $t^* = 26.3$  (red dashed line);  $t^* = 30.1$  (green dash-dotted line);  $t^* = 32.9$  (blue dotted line).

relationship between mole fraction and density as

$$X_{\text{SF}_6} = \frac{\rho - \rho_{\text{air}}}{\rho_{\text{SF}_6} - \rho_{\text{air}}} \quad (40)$$

or

$$\rho = (\rho_{\text{SF}_6} - \rho_{\text{air}})X_{\text{SF}_6} + \rho_{\text{air}}, \quad (41)$$

where  $\rho_{\text{air}}$  and  $\rho_{\text{SF}_6}$  are time-dependent densities of air and SF<sub>6</sub>, respectively, on either side of the material interface from the solutions of the 1D flow representation.  $\rho_{\text{air}}$  and  $\rho_{\text{SF}_6}$  only change at first shock and reshock. Figure 9 compares the ratios between the density mean profiles reconstructed from the mole fraction mean profiles using Eq. (41) and the true density mean profiles for the 2D and 3D cases with physical transport coefficients at different times. The density ratios have less than 5% deviation from one at all times for both 2D and 3D cases, as the flow is quasi-incompressible and the ratio  $p/T$  does not vary much inside the mixing regions. The quasilinear relationship between mole fraction and density suggests that mole fraction field can be viewed as normalized density field within the mixing region.

To quantify the non-Boussinesq effects inside the mixing layer, we can study the effective Atwood number,  $At_e$ , within the central part of the mixing layer, which is defined by Cook *et al.* [49] as

$$At_e = \left\langle \frac{\sqrt{\rho'^2}}{\bar{\rho}} \right\rangle. \quad (42)$$

The Boussinesq approximation is invalid if  $At_e \geq 0.05$ . Since the flows are nearly incompressible, the effective Atwood number is in fact also related to the mole fraction through Eq. (41):

$$At_e \approx \left\langle \frac{\sqrt{X'_{\text{SF}_6}{}^2}}{\bar{X}_{\text{SF}_6} + \rho_{\text{air}}/(\rho_{\text{SF}_6} - \rho_{\text{air}})} \right\rangle. \quad (43)$$

Figure 10 shows the effective Atwood number computed with Eq. (42) against time. Before first shock,  $At_e$  is small and very different from the Atwood number of a discontinuous interface (0.68),



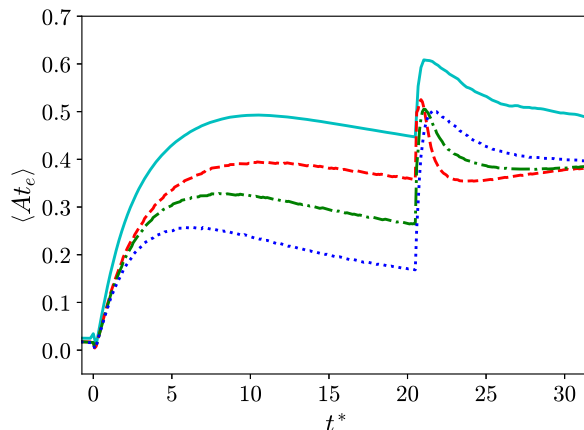


FIG. 10. Comparison of the time evolution of means of effective Atwood number,  $\langle At_e \rangle$ , in the central part of mixing layer between the 2D and 3D problems. Cyan solid line, 2D with physical transport coefficients; red dashed line, 3D with physical transport coefficients; green dash-dotted line, 3D with  $2\times$  physical transport coefficients; blue dotted line, 3D with  $4\times$  physical transport coefficients.

since the material interface is smoothed initially. However, after first shock,  $At_e$  increases rapidly as the interface becomes sharper, followed by gradual decrease due to molecular diffusion. After reshock, there is a jump in  $At_e$  due to further interface intensification.  $At_e$  seems to plateau at late times in all cases. The flows in all cases are very non-Boussinesq after the first shock. In general, the mixing layer is more non-Boussinesq in the 2D configuration than in the 3D configuration, as  $At_e$  is always larger for the 2D case.

### B. Visualization of mole fraction fields

Figures 11 and 12 show the  $SF_6$  mole fraction fields for the 2D and 3D problems at different normalized times  $t^*$ . The development of the bubble and spike structures is very similar at early times after first shock for both cases. As time evolves, the differences in the development of the instability become more distinguishable. In the 2D case, many mushroom structures, which are caused by the rollup of the interface due to baroclinic torque, can be observed. In the 3D case, the rollup of the interface is less prominent. Instead, the bubble and spike grow into long structures at the moment just before reshock. Right after reshock, at  $t^* \approx 21.5$ , there is an immediate enhancement in mixing for both cases. However, the distinction between the 2D and 3D cases remains clear. In the 3D case, particular structures can no longer be identified, which is indicative of the mixing transition. On the contrary, distinct mushroom dipole structures can still be observed for the 2D case, although the flow field becomes much more chaotic than the state just before reshock.

Figures 12, 13, and 14 compare the  $SF_6$  mole fraction fields from the 3D simulations with different transport coefficients. Before reshock, features are smeared out for cases with increased transport coefficients, as the viscous and diffusive effects are acting on faster timescales relative to those of the inviscid linear and nonlinear instability effects. After reshock, the mixing transitions are delayed for the reduced Reynolds number cases. This is most clear for the case with fourfold increase in transport coefficients. Right after reshock, at  $t^* = 22.6$ , features maintaining coherence can still be observed. Nevertheless, based on the visual inspection of the figures, turbulent mixing is observed at the end times for all simulations, indicating that mixing transitions occur in all cases.

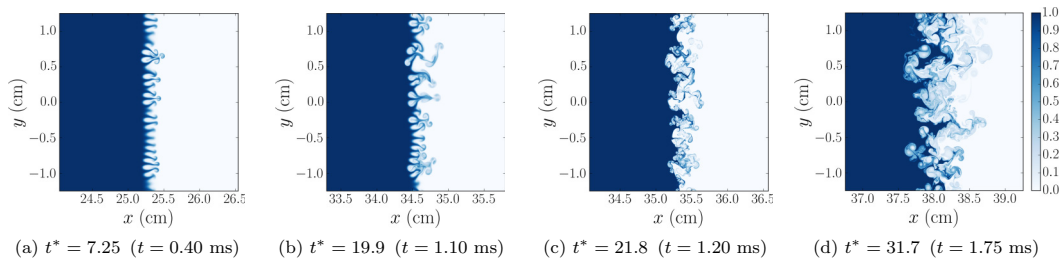


FIG. 11.  $\text{SF}_6$  mole fraction fields,  $X_{\text{SF}_6}$ , at different times from one of the realizations for the 2D problem computed with grid G.

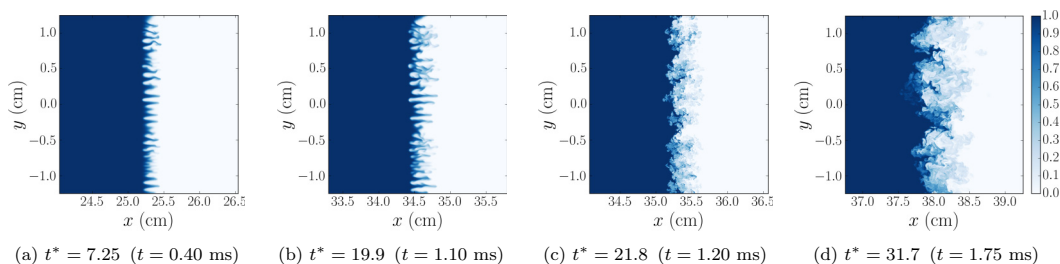


FIG. 12.  $\text{SF}_6$  mole fraction fields,  $X_{\text{SF}_6}$ , in  $xy$  plane at  $z = 0$ , at different times for the 3D problem with physical transport coefficients computed with grid D.

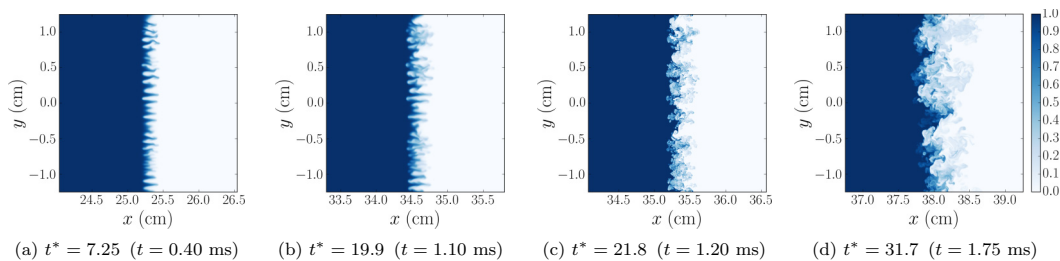


FIG. 13.  $\text{SF}_6$  mole fraction fields,  $X_{\text{SF}_6}$ , in  $xy$  plane at  $z = 0$ , at different times for the 3D problem with  $2\times$  physical transport coefficients computed with grid D.

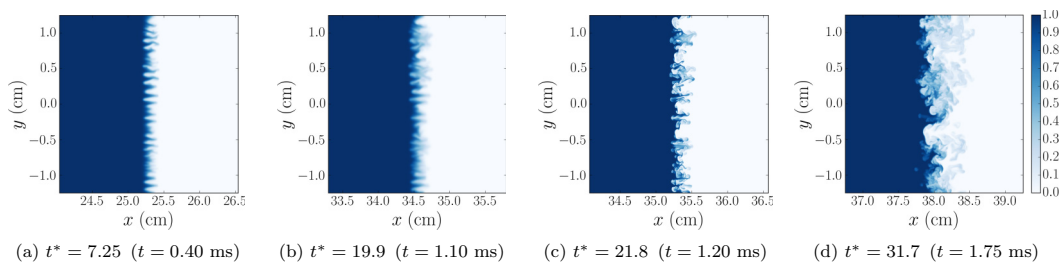


FIG. 14.  $\text{SF}_6$  mole fraction fields,  $X_{\text{SF}_6}$ , in  $xy$  plane at  $z = 0$ , at different times for the 3D problem with  $4\times$  physical transport coefficients computed with grid D.

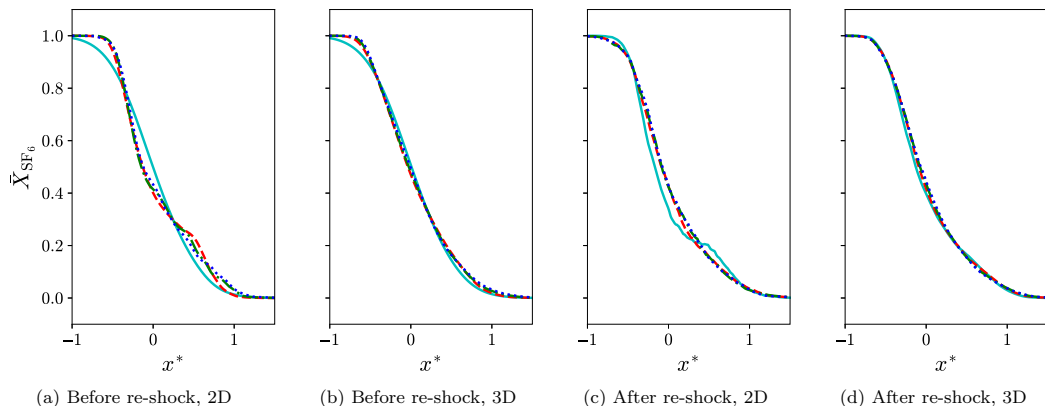


FIG. 15. Profiles of SF<sub>6</sub> mole fraction,  $\bar{X}_{\text{SF}_6}$ , at different times for the 2D and 3D problems with physical transport coefficients. Before reshock:  $t^* = 0.91$  (cyan solid line);  $t^* = 7.25$  (red dashed line);  $t^* = 13.6$  (green dash-dotted line);  $t^* = 19.9$  (blue dotted line). After reshock:  $t^* = 21.8$  (cyan solid line);  $t^* = 25.4$  (red dashed line);  $t^* = 29.0$  (green dash-dotted line);  $t^* = 31.7$  (blue dotted line).

### C. Mole fraction profiles and mixing widths

Figure 15 shows the mean profiles of SF<sub>6</sub> mole fraction,  $\bar{X}_{\text{SF}_6}$ , from the 2D and 3D simulations with physical transport coefficients at different times. The mean mole fraction profiles collapse quite well at late times after both first shock and reshock for both 2D and 3D cases. The profiles are asymmetric, as the spikes penetrate more than the bubbles. Similar findings were also observed for the density profiles in the planar Rayleigh-Taylor (RT) instability, or RTI, studied by Livescu *et al.* [50,51]. It is also interesting to see that the normalized density profiles at late times become quite indistinguishable for both 2D and 3D cases.

The development of the mixing widths for the 2D and 3D cases is compared in Fig. 16(a). The mixing width is normalized by  $\dot{\eta}_{\text{imp}}$  and  $\tau_c$ :

$$W^* = \frac{W - W|_{t=0}}{\dot{\eta}_{\text{imp}} \tau_c}. \quad (44)$$

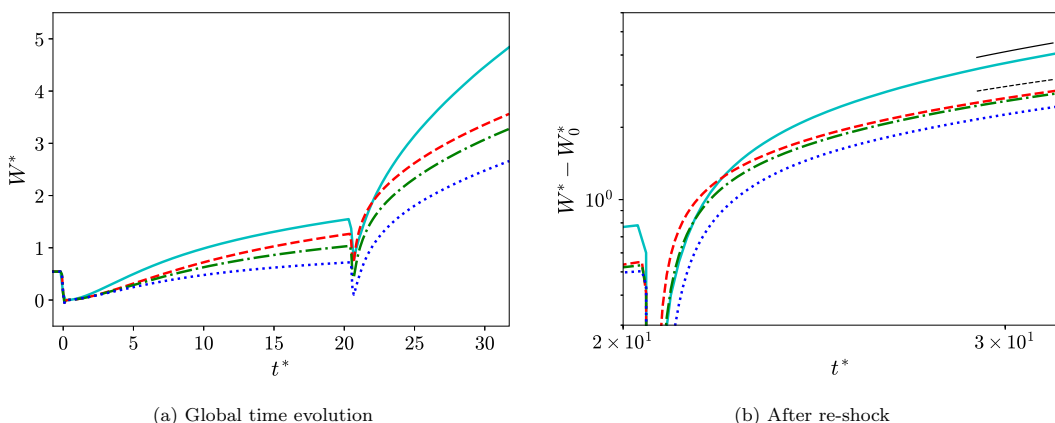


FIG. 16. Comparison of the time evolution of mixing widths between the 2D and 3D problems. Cyan solid line, 2D with physical transport coefficients; red dashed line, 3D with physical transport coefficients; green dash-dotted line, 3D with  $2\times$ physical transport coefficients; blue dotted line, 3D with  $4\times$ physical transport coefficients. The black thin solid and dashed lines indicate the scalings,  $\sim(t^* - t_0^*)^{0.55}$  and  $\sim(t^* - t_0^*)^{0.44}$  respectively, where  $t_0^* = 20.5$  is the reshock time.

With physical transport coefficients,  $W^*$  initially grows at a slightly faster rate in the 2D case compared to the 3D case after first shock, but the growth rates become similar before reshock. After reshock, the 2D mixing width grows at a much higher rate than the 3D mixing width until the end of simulations. Comparing the 3D cases with different transport coefficients on the same figure, it can be seen that although the growths of the normalized mixing widths are very similar just after first shock, they become smaller with decreasing Reynolds number until reshock. After reshock, the growth rates that are different initially become very similar near the end of simulations among all 3D cases, and this can be seen from Fig. 16(b).

In many previous works of RMI, the relation between the turbulent mixing layer width and time was commonly studied through the scaling law  $W^* \sim (t^* - t_0^*)^\theta$ , where  $t_0^*$  is the virtual time origin that is normally chosen as the time when the shock traverses the interface. With that scaling, a wide range of asymptotic values for the exponent  $\theta$  between 0.25 to 0.67 [20,21,52–55] was suggested from theoretical analysis or observed from experiments and simulations. Here, we are mainly interested in how the mixing widths grow at late times after reshock. It is found that at late times after reshock there are reasonable fits for both the 2D and 3D mixing widths using a modified scaling law,  $W^* - W_0^* \sim (t^* - t_0^*)^\theta$ , where  $W_0^*$  is the mixing width at reshock time and  $t_0^*$  is the reshock time. This scaling law, originally proposed by Weber *et al.* [45], leads to better convergence for  $\theta$  over time for both 2D and 3D cases compared to another scaling law mentioned above. We believe both scaling laws should agree with each other at very late times, when  $W^* \gg W_0^*$ . However, this cannot be verified for our cases here as our simulations are constrained by the second reshock. As an additional consistency check on the results, similar values are obtained using a nonlinear fit with  $W_0^*$  and  $t_0^*$  as unknowns, as well as estimating the scalings from derivatives of the mixing widths, without knowledge of  $W_0^*$  and  $t_0^*$  [6]. The  $\theta$  values are estimated to be 0.55 and 0.44, respectively, for the 2D and 3D cases with physical transport coefficients. The  $\theta$  value for the 2D case falls between  $\theta \approx 0.48$  and  $\theta \approx 0.63$  observed from the 2D single-shocked RMI simulations with narrowband and broadband initial conditions, respectively, by Thornber and Zhou [26]. Tritschler *et al.* [21] reported  $\theta \approx 0.29$  at late times after reshock from their 3D RMI simulations with different numerical methods. In the paper by Thornber *et al.* [8], the authors proposed that there is an intermediate stage in time where  $\theta = 0.4$  before  $\theta$  becomes 0.26 at the latest time after reshock and this may explain the discrepancy between the values found for  $\theta$ . The comparison of mixing width time evolution with 2D and 3D scaling laws after reshock is shown in Fig. 16(b).

#### D. Mixedness and mole fraction variance profiles

The time evolution of mixedness is different for the 2D and 3D cases, as seen in Fig. 17. After first shock, from  $t^* = 0$  to  $t^* = 5$ , the mixedness decreases for all cases, as the interface stretches due to rapid gradient intensification, while molecular diffusion is not fast enough to counteract this process. With physical transport coefficients, the 2D mixedness decreases at a faster rate than the 3D mixedness after first shock. At later times after first shock and before the reshock, the mixedness of all cases increases again, as the rate of molecular mixing becomes larger than the rate of entraining pure fluids. Comparing the 3D cases before reshock, it can be seen that mixedness increases with decreasing Reynolds number because of larger molecular diffusion inside the mixing region. After reshock, there is a sudden decrease in mixedness in all cases as the interface stretches again due to gradient intensification. However, the mixedness recovers soon after the sudden reduction of mixedness in all cases. Comparing the 2D and 3D cases with physical transport coefficients, mixedness of the 3D case increases at a faster rate. This is likely associated with turbulent mixing in the 3D case, while transition to turbulence is absent in the 2D case. At late times after reshock, mixedness for all 3D cases seems to approach the same asymptotic value of around 0.8. For the 2D case, the mixedness approaches a different value between 0.65 and 0.7. Similar asymptotic values of mixedness in 3D configurations were observed in previous studies. Lombardini *et al.* [20] and Tritschler *et al.* [21] found that the mixedness in their simulations approached 0.85 asymptotically.

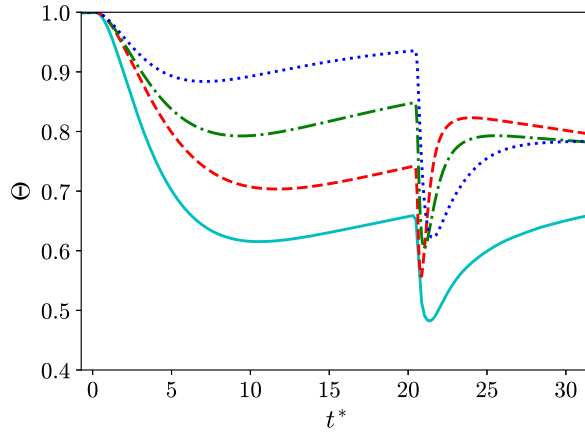


FIG. 17. Comparison of the time evolution of mixedness between the 2D and 3D problems. Cyan solid line, 2D with physical transport coefficients; red dashed line, 3D with physical transport coefficients; green dash-dotted line, 3D with  $2\times$ physical transport coefficients; blue dotted line, 3D with  $4\times$ physical transport coefficients.

Mohaghar *et al.* [16] also found an asymptotic value of 0.8 for mixedness in their experimental study. As for the 2D configuration, Thornber and Zhou [26] found an asymptotic value of 0.63 for mixedness in their 2D single-shocked simulations with narrowband initial perturbations. The mixedness of the 2D case is smaller than that of the 3D case with physical transport coefficients at all times. This suggests that fluids are less molecularly mixed in the 2D configuration. The difference in mixedness between the 2D and 3D cases becomes larger after reshock, which is probably due to lack of turbulence to enhance mixing in the 2D case.

Mixing can be further studied through the spatial profiles of mole fraction variance. Smaller variance indicates a larger extent of molecular mixing, as the fluid regions are more homogeneous. In fact, mixedness can be related to the spatial profile of mole fraction variance, by rewriting Eq. (28) as

$$\Theta = 1 - 4 \frac{\int \overline{X_{SF_6}^2} dx}{W} = 1 - 4 \int \overline{X_{SF_6}^2} dx^*. \quad (45)$$

Figure 18 shows the profiles of  $SF_6$  mole fraction variance,  $\overline{X_{SF_6}^2}$ , across the normalized position  $x^*$  from the 2D and 3D simulations with physical transport coefficients at different times. All profiles have peaks on the heavier fluid side, which indicates that fluids mix more slowly on the heavier fluid side for this variable-density flow. Similar asymmetries were also observed in other flows with strong variable-density effects [51,56,57], where they were associated with different inertia of the light and heavy fluid regions. Comparing 2D and 3D profiles at different times, the profile peaks are always larger in the 2D case and this is consistent with the smaller mixedness values for the 2D case. After reshock, the profiles become more self-similar for both 2D and 3D cases at late times, consistent with the mixedness approaching asymptotic limits. This also suggests that a balanced state between entrainment of pure fluids at the edges of mixing layer and molecular mixing is approximately obtained in both configurations at late times. A similar balanced state was observed in freely decaying variable-density turbulence starting from isotropic turbulent fields by Movahed and Johnsen [58].

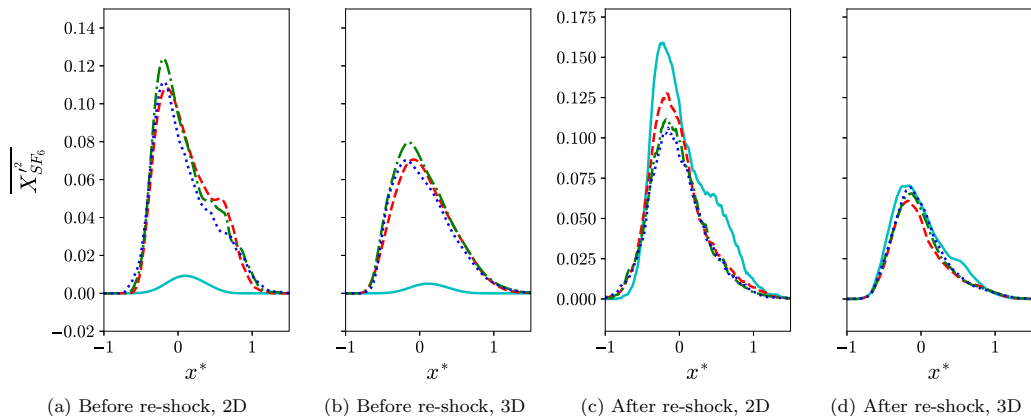


FIG. 18. Profiles of SF<sub>6</sub> mole fraction variance,  $\overline{X_{SF_6}^2}$ , at different times for the 2D and 3D problems with physical transport coefficients. Before reshock:  $t^* = 0.91$  (cyan solid line);  $t^* = 7.25$  (red dashed line);  $t^* = 13.6$  (green dash-dotted line);  $t^* = 19.9$  (blue dotted line). After reshock:  $t^* = 21.8$  (cyan solid line);  $t^* = 25.4$  (red dashed line);  $t^* = 29.0$  (green dash-dotted line);  $t^* = 31.7$  (blue dotted line).

### E. Probability density functions of mole fraction

The discrete probability density function (PDF) of a quantity  $\phi$  bounded by  $\phi_{\min}$  and  $\phi_{\max}$  for the  $k$ th bin, where  $k \in [1, 2, \dots, N_b]$ , can be computed with

$$\text{PDF} = \frac{N_k}{(\Delta\phi)N}, \quad (46)$$

where  $N$  and  $N_k$  are the total number of cells and the number of cells for the  $k$ th bin in the central part of mixing layer respectively.  $\Delta\phi$  is given by

$$\Delta\phi = \frac{\phi_{\max} - \phi_{\min}}{N_b}, \quad (47)$$

where  $N_b$  is the total number of bins.

The PDF's of SF<sub>6</sub> mole fraction at different times for 2D and 3D cases are compared in Fig. 19 before reshock and Fig. 20 after reshock. For the 3D case with physical transport coefficients, it can be seen that the PDF has a quasi-Gaussian shape immediately after first shock resulting from the initial smooth profile of the material interface. However, as pure fluids are being entrained into the central part of mixing layer, two peaks at the pure fluid ends appear. As the instability evolves and the molecular effects start dominating the entrainment, the amplitude of each peak diminishes. With increased transport coefficients or reduced Reynolds number, the peaks at the pure fluid ends can no longer be clearly observed at late times after first shock. The evolution of the PDF for the 2D case is very similar to that for the 3D case with physical transport coefficients, but there seems to be more entrainment over time and the molecular diffusion effect is smaller. This is consistent with previous results that fluids in the 2D configuration are less mixed than those in 3D configuration before reshock.

After reshock, there is a common fundamental change in each mole fraction PDF. For each case, the PDF returns to a unimodal shape in the central region of  $X_{SF_6}$  values; however, this shape is strongly asymmetric, with the peak in the light fluid region and elongated tail in the heavy fluid region. Moreover, shortly after reshock, each PDF has two additional peaks near the two pure fluid values. At later times, only the heavy fluid peak ( $X_{SF_6} \sim 1$ ) survives. The same form was also noticed for the density PDF of Hill *et al.* [18] and mass fraction PDF of Tritschler *et al.* [21] from 3D simulations. The similar shape of the PDF's indicates that each flow is composed of moderately

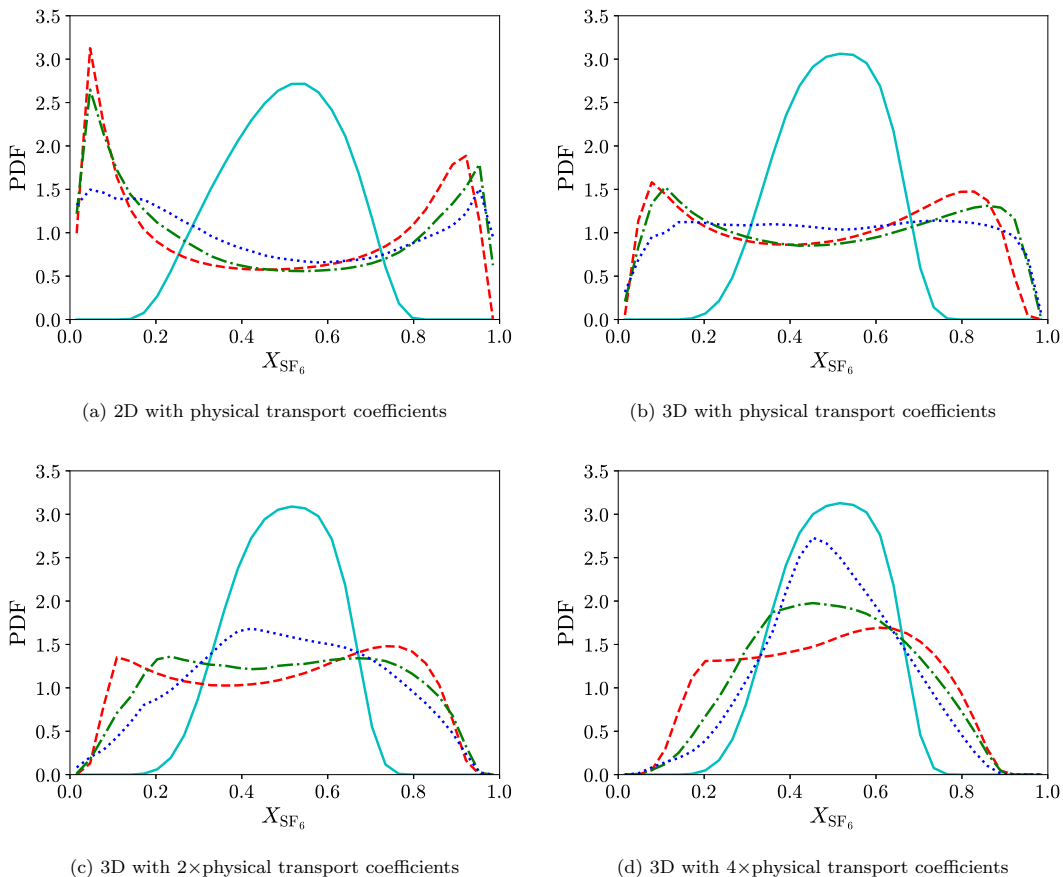


FIG. 19. PDFs of  $\text{SF}_6$  mole fraction,  $X_{\text{SF}_6}$ , for the 2D and 3D problems before reshock. Cyan solid line,  $t^* = 0.91$ ; red dashed line,  $t^* = 7.25$ ; green dash-dotted line,  $t^* = 13.6$ ; blue dotted line,  $t^* = 19.9$ .

mixed regions of lighter than average fluid and some pure regions of heavier fluid. At later times, the pure light fluid regions are significantly reduced but significant pure heavy fluid regions are still present. The same effect was also observed in other variable-density flows, such as homogeneous RTI by Livescu and Ristorcelli [56], classical RTI by Livescu *et al.* [50,51], variable-density round jet by Gerashchenko and Prestridge [59], and variable-density shock-turbulence interaction by Tian *et al.* [57]. The central peak of the PDF shifts even more toward the lighter fluid side with smaller Reynolds number, which could be attributed to smaller baroclinic torque generated from smaller perturbation amplitude at reshock. Thus, the subsequent reduced stirring makes it more difficult for the higher inertia and heavier fluid to mix.

### F. Turbulent kinetic energy and Reynolds stress anisotropy

Figure 21(a) compares the time evolution of mean TKE in the central part of the mixing layer,  $\overline{\langle \text{TKE} \rangle}$ , between the 2D and 3D cases. The mean TKE is normalized in each case such that it is equal to one at  $t^* = 0$  for better comparison between different cases. From Fig. 21(a), it can be seen that after first shock, there is a sudden jump in the TKE value for each case. Comparing the 2D and 3D cases with physical transport coefficients, the mean TKE decays after the jump, with similar decay rates for both cases until  $t^* \approx 3$ . At later times, TKE decays at a faster rate for the 3D case. This is likely associated with the presence of the vortex stretching mechanism in 3D domain, which

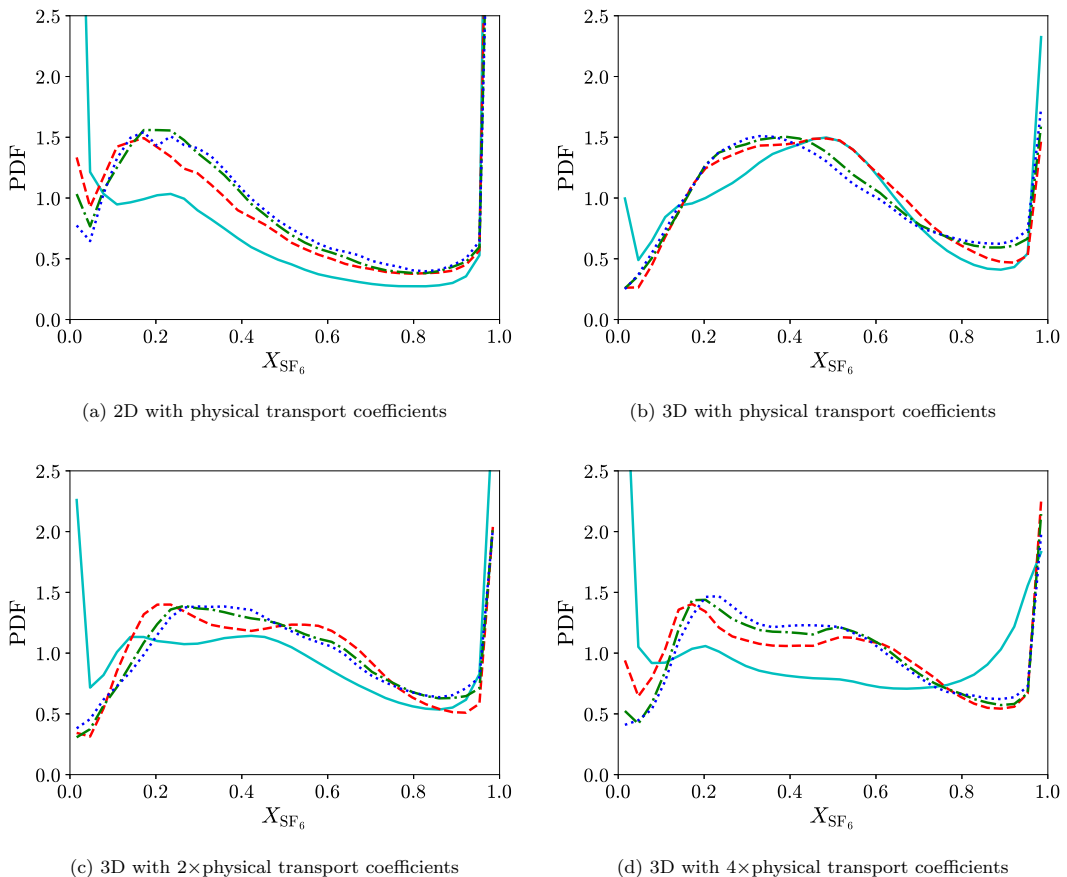


FIG. 20. PDFs of  $\text{SF}_6$  mole fraction,  $X_{\text{SF}_6}$ , for the 2D and 3D problems after reshock. Cyan solid line,  $t^* = 21.8$ ; red dashed line,  $t^* = 25.4$ ; green dash-dotted line,  $t^* = 29.0$ ; blue dotted line,  $t^* = 31.7$ .

enhances the breakdown of large-scale features into smaller scales. After reshock, the distinction in the decay rates between the 2D and 3D cases is much larger, with an even faster decay rate for the 3D case.

Comparing the 3D cases, after first shock, TKE decays more rapidly with smaller Reynolds number (i.e., with larger transport coefficients) and this effect holds until re-shock. After reshock, although the decay rates are different among the cases initially, they become very similar and almost identical at late times. This is evident from Fig. 21(b), which only shows the temporal decay of the normalized mean TKE after reshock for different cases. We have also examined the scaling law after reshock for TKE,  $\sim (t^* - t_0^*)^{-n}$ , that was investigated in many previous studies [20,21,60]. Similar to the study of scaling law for mixing widths, we have chosen  $t_0^*$  to be the reshock time. This choice was also verified using a nonlinear curve fitting with unknown  $t_0^*$ . At late times after reshock, the values of  $n$  for 2D and 3D cases with physical transport coefficients approach 0.5 and 1.4, respectively. The comparison of TKE time evolution with the 2D and 3D scaling laws after reshock can be seen in Fig. 21(b). The value of  $n$  found for the 3D case is essentially as same as the value  $n = 10/7 \approx 1.42$  observed by Tritschler *et al.* [21] after reshock from their 3D simulations. Lombardini *et al.* [20] also reported that the value of  $n$  was close to  $10/7$  at late times of their single-shocked simulations. A TKE scaling with  $n = 10/7$  is identical to the TKE scaling of decaying turbulence of Batchelor-type [61], in contrast to that of Saffman-type [62,63] with  $n = 6/5$ .



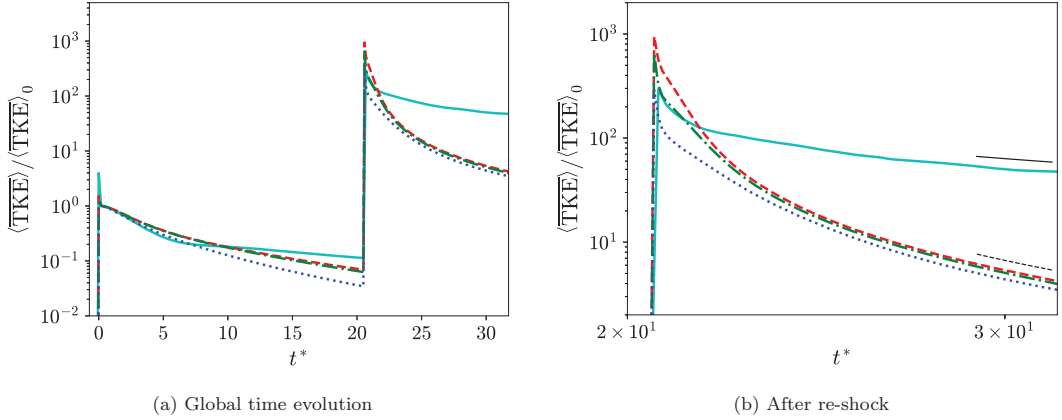


FIG. 21. Comparison of the time evolution of the normalized means of turbulent kinetic energy, TKE, in the central part of mixing layer between the 2D and 3D problems. Mean TKE is normalized by its value at  $t^* = 0$ ,  $\langle \text{TKE} \rangle_0$ . Cyan solid line, 2D with physical transport coefficients; red dashed line, 3D with physical transport coefficients; green dash-dotted line, 3D with  $2 \times$  physical transport coefficients; blue dotted line, 3D with  $4 \times$  physical transport coefficients. The black thin solid and dashed lines indicate the scalings,  $\sim (t^* - t_0^*)^{-0.5}$  and  $\sim (t^* - t_0^*)^{-1.4}$  respectively, where  $t_0^* = 20.5$  is the reshock time.

Figure 22 compares the mean profiles of TKE at different times for the 2D and 3D cases with physical transport coefficients. Before averaging in the homogeneous directions to get the mean profiles, TKE is first normalized as

$$K^* = \frac{\langle \text{TKE} \rangle W}{\int \text{TKE} dx}. \quad (48)$$

Except at the very early times, the normalized TKE profiles approximately collapse when comparing the profiles at later times after both the first shock and reshock, with only some small variation in the magnitude of the peak. Before reshock, TKE peaks on the light fluid side ( $x^* > 0$ ) for both 2D and 3D cases, as mixing is more prominent on this side and this is consistent with

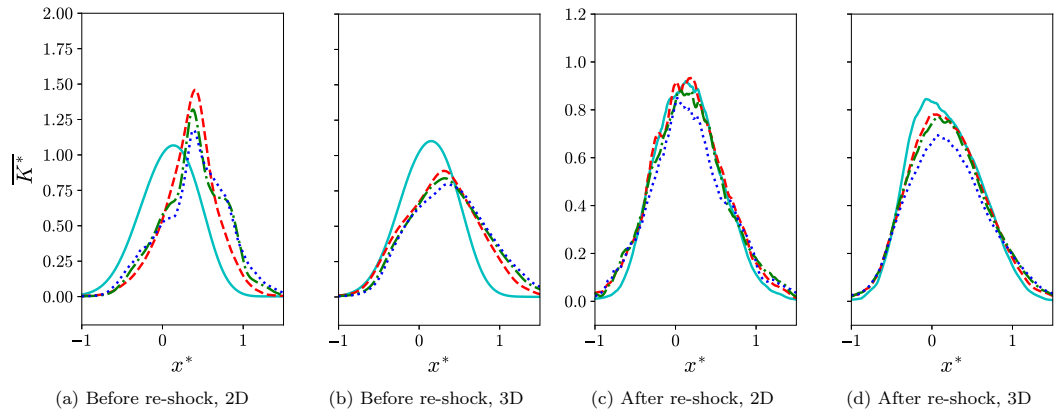


FIG. 22. Profiles of normalized turbulent kinetic energy at different times for the 2D and 3D problems with physical transport coefficients. Before reshock:  $t^* = 0.91$  (cyan solid line);  $t^* = 7.25$  (red dashed line);  $t^* = 13.6$  (green dash-dotted line);  $t^* = 19.9$  (blue dotted line). After reshock:  $t^* = 21.8$  (cyan solid line);  $t^* = 25.4$  (red dashed line);  $t^* = 29.0$  (green dash-dotted line);  $t^* = 31.7$  (blue dotted line).

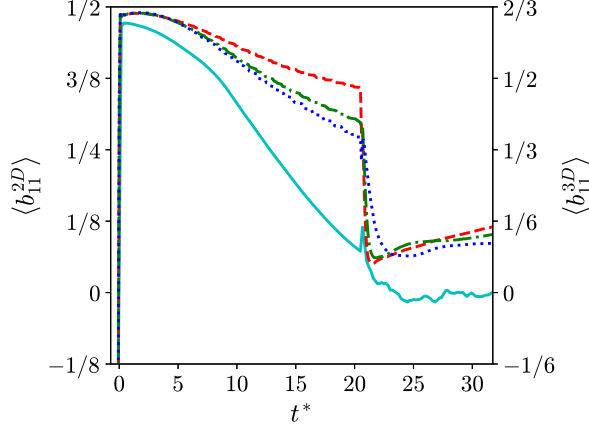


FIG. 23. Comparison of the time evolution of the means of Reynolds stress anisotropy component,  $\langle b_{11} \rangle$ , in the central part of mixing layer between the 2D and 3D problems. Cyan solid line, 2D with physical transport coefficients; red dashed line, 3D with physical transport coefficients; green dash-dotted line, 3D with  $2\times$  physical transport coefficients; blue dotted line, 3D with  $4\times$  physical transport coefficients.

the mole fraction variance profiles. The TKE peak in the 2D case is higher than that in the 3D case, which means TKE is more localized toward the light fluid side under the 2D configuration. However, after reshock, the peaks of mean  $K^*$  for both cases move closer to the midline or midplane ( $x^* = 0$ ) of the mixing layer and the shapes of the profiles for the 2D and 3D problems look more similar.

Besides TKE, the Favre-averaged Reynolds stress anisotropy tensor,  $b_{ij}$ , is another statistical quantity of interest from the velocity field. The 2D and 3D anisotropy tensors,  $b_{ij}^{2D}$  and  $b_{ij}^{3D}$ , are defined as

$$b_{ij}^{2D} = \frac{\tilde{R}_{ij}}{\tilde{R}_{kk}} - \frac{1}{2}\delta_{ij}, \quad (49)$$

$$b_{ij}^{3D} = \frac{\tilde{R}_{ij}}{\tilde{R}_{kk}} - \frac{1}{3}\delta_{ij}, \quad (50)$$

where  $\delta_{ij}$  is the Kronecker  $\delta$  and  $\tilde{R}_{ij}$  is the Favre-averaged Reynolds stress tensor given by

$$\tilde{R}_{ij} = \frac{\overline{\rho u_i'' u_j''}}{\bar{\rho}}. \quad (51)$$

$b_{11}^{2D}$  and  $b_{11}^{3D}$  indicate the amount of TKE contributed from the streamwise component of Reynolds normal stresses.  $b_{11}^{2D} = 1/2$  and  $b_{11}^{3D} = 2/3$  correspond to having all TKE contributed from  $\bar{\rho}\tilde{R}_{11}/2$ , while  $b_{11}^{2D} = -1/2$  and  $b_{11}^{3D} = -1/3$  mean that there is no contribution to TKE from that component. The Reynolds normal stresses are isotropic if  $b_{11}^{2D} = 0$  in 2D flow or  $b_{11}^{3D} = 0$  in 3D flow.

Figure 23 shows the time evolution of mean  $b_{11}$  in the central part of mixing layer for the 2D and 3D cases. In all cases, the means of  $b_{11}$  almost attain their maximum values of  $1/2$  and  $2/3$  for the 2D and 3D cases, respectively, right after first shock. This is followed by a reduction of  $\langle b_{11} \rangle$  until just before reshock. However, comparing cases with the physical transport coefficients,  $\langle b_{11} \rangle$  decreases more rapidly for the 2D case. Since the kinetic energy decays slower for the 2D case, the faster return toward isotropy for this case can be associated with a more efficient TKE redistribution among the Reynolds normal stresses. For quasi-incompressible flows, this redistribution is largely associated with the pressure-strain terms [64] in the Reynolds stress tensor transport equation. Thus,

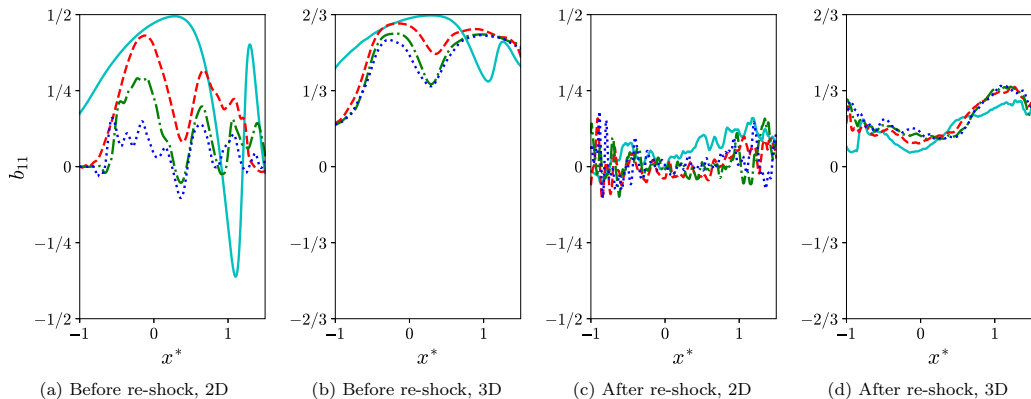


FIG. 24. Profiles of Reynolds stress anisotropy component,  $b_{11}$ , at different times for the 2D and 3D problems with physical transport coefficients. Before reshock:  $t^* = 0.91$  (cyan solid line);  $t^* = 7.25$  (red dashed line);  $t^* = 13.6$  (green dash-dotted line);  $t^* = 19.9$  (blue dotted line). After reshock:  $t^* = 21.8$  (cyan solid line);  $t^* = 25.4$  (red dashed line);  $t^* = 29.0$  (green dash-dotted line);  $t^* = 31.7$  (blue dotted line).

Fig. 23 implies a stronger pressure-strain correlation for the 2D case as the flow evolves after the interaction with the shock.

At reshock, there is a sudden decline in  $\langle b_{11} \rangle$  values for all cases. For the 2D case,  $\langle b_{11} \rangle$  reaches the isotropic value of zero rapidly after reshock, while for the 3D cases, the TKE fields remain anisotropic until the end of simulations. Thornber and Zhou [26] also noticed rapid isotropization of the Reynolds normal stresses from their narrowband 2D simulations compared to the 3D cases. Both results concerning the 3D cases by Lombardini *et al.* [20] and Tritschler *et al.* [21] show slow isotropization of the Reynolds normal stresses over a long period of time and small nonzero asymptotic limits in anisotropy were observed. The Reynolds normal stresses in our 3D simulations still remain very anisotropic at late times compared to the asymptotic limit in Tritschler *et al.* [21], probably because of a shorter time duration from reshock time to the end of simulation constrained by the arrival of the second reshock. Comparing the time evolution of  $\langle b_{11} \rangle$  among different 3D cases, there is a slightly smaller anisotropy before reshock at lower Reynolds numbers, as diffusive effects are more important before the flows become fully turbulent. After reshock, all 3D cases have similar anisotropy.

Figure 24 compares the mean profiles of  $b_{11}$  at different times for the 2D and 3D cases with physical transport coefficients. After first shock, as the flow remains transitional,  $\langle b_{11} \rangle$  varies a lot inside the mixing layer for both 2D and 3D cases. However, consistent with Fig. 23, the overall profile for the 2D case is approaching zero at faster rate. After reshock,  $b_{11}$  has become more uniform inside the mixing layer for both 2D and 3D cases. However, for the 3D case, there is a slight asymmetry between the light and heavy fluid sides, with larger anisotropy on the light fluid side ( $x^* > 0$ ). As seen above, the kinetic energy is larger on the light fluid side, which corresponds to higher Reynolds numbers. Consistent with the time variation of  $\langle b_{11} \rangle$ , its local values also remain larger at higher Reynolds numbers.

### G. Spectra

Figure 25 shows the spectra of SF<sub>6</sub> mole fraction,  $\langle E_{X_{SF_6}} \rangle$ , at different times after reshock computed within the central part of mixing layer for both 2D and 3D cases with physical transport coefficients. At the end time of the simulations, inertial ranges are emerging for both cases. The scaling in the inertial range is close to  $\langle E_{X_{SF_6}} \rangle \propto k^{-5/3}$  for the 2D case and close to  $\langle E_{X_{SF_6}} \rangle \propto k^{-3/2}$  for the 3D case. The scaling of mole fraction spectrum at the end of 3D simulation is close to that of density spectra observed by Tritschler *et al.* [21] in their 3D RMI simulations at early times after

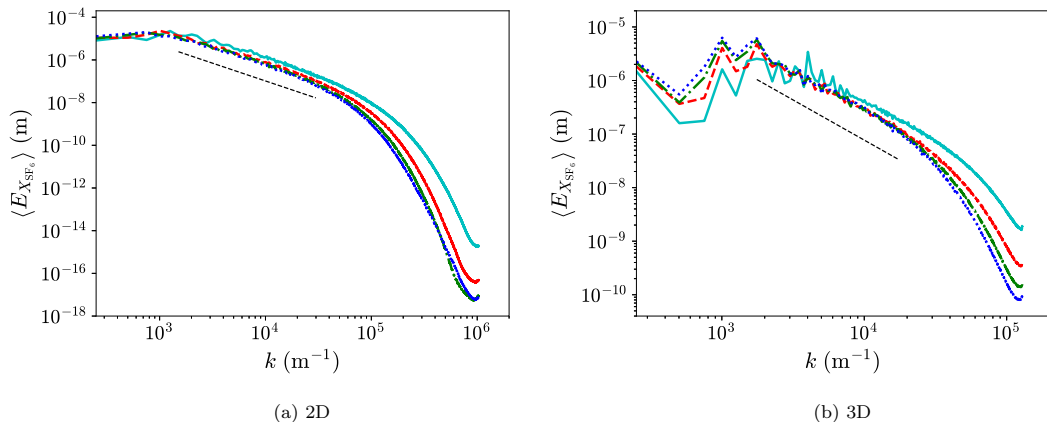


FIG. 25. Spectra of  $\text{SF}_6$  mole fraction,  $X_{\text{SF}_6}$ , at different times after reshock for the 2D and 3D problems with physical transport coefficients in the central part of mixing layer. Thin black dashed line,  $k^{-5/3}$  or  $k^{-3/2}$  (2D or 3D); cyan solid line,  $t^* = 21.8$ ; red dashed line,  $t^* = 25.4$ ; green dash-dotted line,  $t^* = 29.0$ ; blue dotted line,  $t^* = 31.7$ .

reshock, although long after reshock they found a smaller gradient scaling for the spectra. Weber *et al.* [65] reported a  $-5/3$  scaling for the mole fraction spectra from their 3D RMI experimental results at late times but the experiments did not have reshock.

To study the energy spectrum in variable-density or compressible turbulence, it is common to decompose the energy as  $|\sqrt{\rho}\mathbf{u}'|^2$  or  $|\sqrt{\rho}\mathbf{u}''|^2$  [56,66–68]. However, it is pointed out by Zhao and Aluie [69] that one cannot prove spectral locality using energy definitions of the form  $|\sqrt{\rho}\mathbf{u}'|^2$ , because the corresponding transport equations contain terms that are divided by  $\sqrt{\rho}$  and can no longer be arranged in divergence form. As a result, viscous effects may not decay at large scales when density variations are large. This lack of locality prevents the corresponding energy from developing an inertial range. Instead, they suggested that kinetic energy defined using Favre (density-weighted) filtering,  $\hat{\rho}|\hat{\mathbf{u}}|^2$ , where  $\hat{\cdot}$  and  $\tilde{\cdot}$  represent the simple and Favre filtering respectively, can develop an inertial range. While useful for proving locality of energy transfer in the context of filtering, this quantity is not in quadratic form and thus not the proper way to form the energy spectrum. The energy spectrum based on  $|\rho\mathbf{u}''/\sqrt{\bar{\rho}}|^2$  energy definition satisfies the requirement that terms in the corresponding transport equations remain in divergence form, while we still have a quadratic form for the energy.

Figure 26 compares the energy spectra computed within the central part of mixing layer with four different energy definitions: (1)  $|\sqrt{\bar{\rho}}\mathbf{u}'|^2$ , (2)  $|\sqrt{\bar{\rho}}\mathbf{u}''|^2$ , (3)  $|\rho\mathbf{u}'/\sqrt{\bar{\rho}}|^2$ , and (4)  $|\rho\mathbf{u}''/\sqrt{\bar{\rho}}|^2$ , for both 2D and 3D cases with physical transport coefficients, at the end of simulations. Energy definitions using  $|\rho\mathbf{u}'/\sqrt{\bar{\rho}}|^2$  and  $|\rho\mathbf{u}''/\sqrt{\bar{\rho}}|^2$  yield spectra that are almost indistinguishable for the flow in each case considered here. Also, switching  $\mathbf{u}'$  and  $\mathbf{u}''$  has unnoticeable effects on the spectra for other two energy definitions. Although the spectra for the 3D case are close with the choices above, the spectra computed with  $|\rho\mathbf{u}'/\sqrt{\bar{\rho}}|^2$  or  $|\rho\mathbf{u}''/\sqrt{\bar{\rho}}|^2$  for the 2D case seem to have clearer inertial range than spectra computed with the other two energy definitions, confirming the discussion above.

Figure 27 shows the energy spectra computed with  $|\rho\mathbf{u}''/\sqrt{\bar{\rho}}|^2$ ,  $\langle E_{\rho\mathbf{u}''/\sqrt{\bar{\rho}}} \rangle$ , at different times for both 2D and 3D cases. As seen from the figure, an inertial range is developing for each case. Comparing the 2D and 3D problems, there is a huge difference in scaling for the spectra in the inertial ranges. The scaling is close to  $\langle E_{\rho\mathbf{u}''/\sqrt{\bar{\rho}}} \rangle \propto k^{-2.7}$  for the 2D case but close to  $\langle E_{\rho\mathbf{u}''/\sqrt{\bar{\rho}}} \rangle \propto k^{-3/2}$  for the 3D case. Thornber and Zhou [26] found the scaling of spectra of kinetic energy defined as  $|\sqrt{\rho}\mathbf{u}'|^2/2$  close to  $E \propto k^{-3}$  at high wave numbers at late times in their inviscid 2D RMI simulations with different initial perturbations. Similar to our results for the 3D case, Tritschler

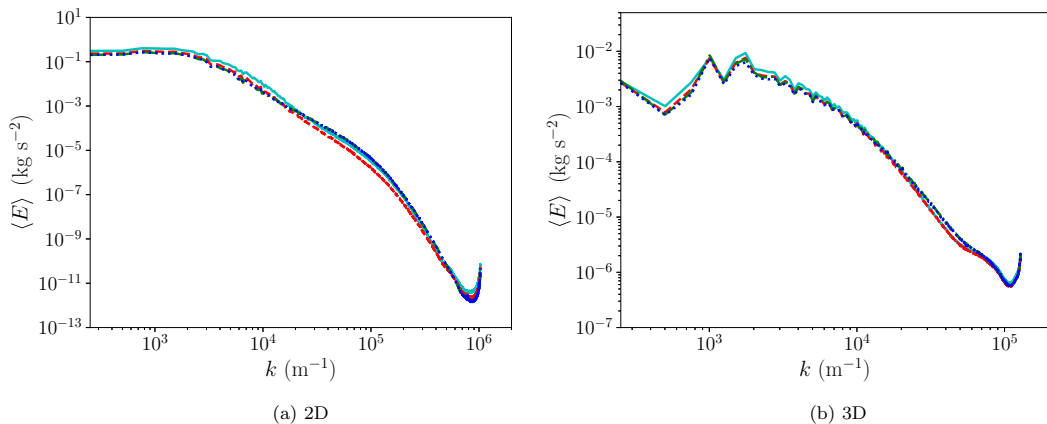


FIG. 26. Energy spectra computed with different energy definitions at the end of simulation ( $t^* = 31.7$ ) for the 2D and 3D problems with physical transport coefficients in the central part of mixing layer. Cyan solid line,  $(\sqrt{\rho}u')^2$ ; red dashed line,  $(\sqrt{\rho}u'')^2$ ; green dash-dotted line,  $(\rho u' / \sqrt{\rho})^2$ ; blue dotted line,  $(\rho u'' / \sqrt{\rho})^2$ .

*et al.* [21] also found scaling of spectra of turbulent kinetic energy defined as  $|\sqrt{\rho}u''|^2/2$  close to  $-3/2$  scaling after reshock from their 3D RMI simulations, although the postreshock 3D simulation results by Lombardini *et al.* [20] show that a  $-5/3$  power law seems to be more appropriate for energy contributed from the streamwise velocity component.

## IX. CONCLUSIONS

We have conducted high-resolution 2D and 3D Navier-Stokes simulations of multispecies mixing driven by RMI. Through grid sensitivity analysis of statistical quantities that are dependent on features of different scales, we have confirmed that the highest grid resolution used for 2D simulations was sufficient to provide accurate statistics that depend on smallest scale features in the flows. Although the highest grid resolution used for 3D simulations is not sufficient to capture statistics that are associated with finest scale features, such as scalar dissipation rate and enstrophy,

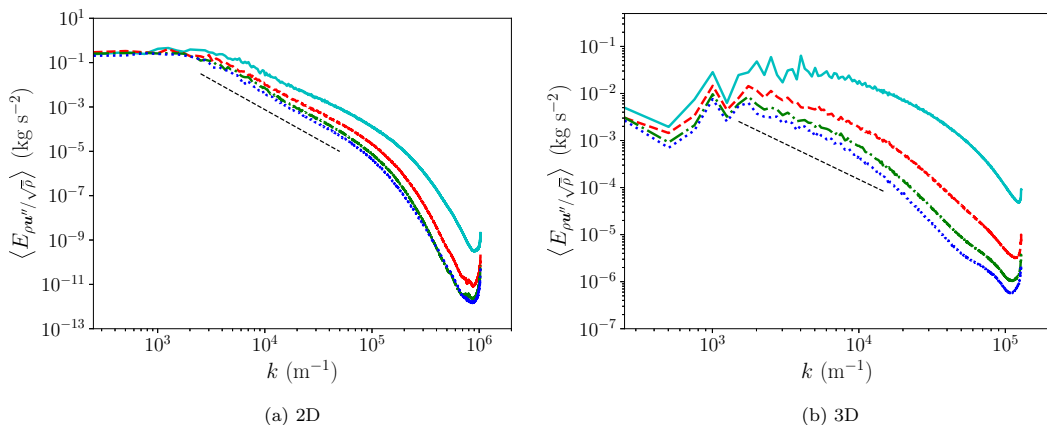


FIG. 27. Energy spectra at different times after reshock for the 2D and 3D problems with physical transport coefficients in the central part of mixing layer. Thin black dashed line,  $k^{-2.7}$  or  $k^{-3/2}$  (2D or 3D); cyan solid line,  $t^* = 21.8$ ; red dashed line,  $t^* = 25.4$ ; green dash-dotted line,  $t^* = 29.0$ ; blue dotted line,  $t^* = 31.7$ .

the grid resolution is high enough for converged statistics that depend on large-scale features, such as mixing width and TKE. It was found that, for the chosen initial configuration, the flows inside the mixing layers were only weakly compressible for most of the time under both 2D and 3D configurations. However, the effective Atwood number within the mixing layer remains high throughout the simulations, leading to noticeable variable-density effects. The importance of these effects could be inferred from the asymmetry in the spatial profiles of mole fraction variance and TKE, and also the mole fraction PDF's.

The mole fraction profiles become self-similar for both 2D and 3D problems after a short transient regime, following both first shock and reshock. However, the mixing layer width grows faster for the 2D case after first shock and reshock. The 2D and 3D scalings of mixing widths at late times after reshock were quantified and compared with previous studies. The results show that the scalings converge, when the thickness of the layer at reshock and time of reshock are included in the scaling law. The scaling exponents for the 2D and 3D problems have been evaluated to be around 0.55 and 0.44, respectively, using different fitting techniques. Similar values have been obtained when calculated directly from the temporal derivatives of the mixing layer widths. Consistent with the differences in the scaling laws, there also appears to be asymptotic but different mixedness values for 2D and 3D problems, where that of the former is smaller. Overall, the temporal evolutions of mixedness and PDF of mole fraction at different times indicate that the fluids are more difficult to mix under the 2D configuration than the 3D configuration.

We have also compared the time evolution of TKE and anisotropy of the Reynolds normal stresses for both configurations. It is clear that without the effect of vortex stretching to break large-scale features into smaller scales, the mean TKE decays more slowly under the 2D configuration. On the other hand, the Reynolds normal stresses become isotropic quickly after reshock for the 2D case, while they remain quite anisotropic under 3D configuration even at late times. Similar to mixing widths, the 2D and 3D scalings of TKE at late times after reshock have been evaluated and the scaling for the 3D problem has been found to be similar to that for Batchelor-type decaying turbulence. This finding is consistent with some of the previous studies on RMI. The 2D and 3D cases have also been compared by considering the evolution of the mole fraction and energy spectra after reshock. Different scalings in inertial ranges for the 2D and 3D spectra can be seen clearly at late times after reshock. The energy spectra are based on a new definition of energy, which is consistent with the inviscid criterion for decomposing scales [69]. While the effect to isolate the viscous effects cannot be seen in the 3D problem due to insufficient grid resolution, there is clearly a longer inertial range for the 2D case with the new definition of energy. This indicates that the new definition may be a more appropriate metric for the spectral analysis of turbulence energy for variable-density flows.

The effects of Reynolds number on 3D RMI have also been analyzed by varying the physical transport coefficients. Through artificially increasing the values of physical transport coefficients given by diffusivity and viscosity models, the Reynolds number based on mixing width or integral length scale is effectively reduced over time. The effect of reduced Reynolds number is small on the growth of mixing layer width, mixedness, and decay rate of TKE at late times after reshock, but greatly affects the development of many statistical quantities between first shock and reshock. During this time, the growth rate of mixing layer width decreases, while the decay rate of TKE increases for cases with smaller Reynolds numbers. At the same time, Reynolds normal stresses become isotropic at faster rate with decreased Reynolds number values. The changes of flow field variables due to Reynolds number effects before the occurrence of mixing transition address the importance of including viscous and diffusive effects in variable-density simulations for accurate predictions of the growth of instabilities.

#### ACKNOWLEDGMENTS

This work was performed under the auspices of U.S. Department of Energy. M. L. Wong and S. K. Lele were supported by Los Alamos National Laboratory, under Grant No. 431679. Los Alamos National Laboratory is operated by Triad National Security, LLC, for the National Nuclear Security

Administration of US Department of Energy (Contract No. 89233218CNA000001). Computational resources were provided by the Los Alamos National Laboratory Institutional Computing Program.

## APPENDIX A: STATISTICAL SENSITIVITY ANALYSIS OF TWO-DIMENSIONAL SIMULATIONS

Figure 28 shows the time evolution of various statistical quantities computed with different number of realizations and the grid G settings for the 2D problem. It can be seen from the figure that statistical convergence has already been obtained for the quantities considered with 24 realizations for all times. The standard deviations of mixing width and TKE (only after reshock) over 24 realizations are also shown in the same figure. The standard deviations of mixing width and TKE are insignificant before reshock. However, after reshock, they have become large and hence statistical convergence can only be obtained for the quantities with a large number of realizations.

## APPENDIX B: PROFILES OF RATIO OF PRESSURE TO TEMPERATURE

Figures 29 and 30 show the normalized mean and standard deviation profiles for the ratio  $p/T$  across the mixing layers at different times for both 2D and 3D problems with physical transport coefficients. The mean profiles are normalized with the pressure ( $p_{\text{SF}_6}$  and  $p_{\text{air}}$ ) and temperature ( $T_{\text{SF}_6}$  and  $T_{\text{air}}$ ) on either side of the material interface from the solutions of the 1D flow representation. The standard deviation profiles are normalized by the mean profiles. It can be seen that the mean profiles at most only have around  $\pm 10\%$  variations across the mixing layers and the normalized standard deviation profiles have magnitudes smaller than 10% at all times. Therefore, the ratios  $p/T$  inside the mixing layers are quasiumiform for both 2D and 3D cases.

## APPENDIX C: TIME EVOLUTION OF LENGTH SCALES AFTER RESHOCK

In this section, the time evolution of different length scales after reshock for the highest Reynolds number 3D case (with physical transport coefficients) are estimated and briefly discussed. According to Pope [70], the Reynolds number associated with the outer-scale (largest scale) eddies,  $\text{Re}_{l_o}$ , can be related to the Taylor-scale Reynolds number,  $\text{Re}_{\lambda_T}$ , with a few assumptions. The Reynolds numbers are given by

$$\text{Re}_{l_o} = \sqrt{\frac{3}{2}} \frac{\rho u_{\text{turb}} l_o}{\mu}, \quad (\text{C1})$$

$$\text{Re}_{\lambda_T} = \frac{\rho u_{\text{turb}} \lambda_T}{\mu}, \quad (\text{C2})$$

where  $l_o$  and  $\lambda_T$  are the length scale of the largest eddies and Taylor microscale, respectively. The characteristic velocity scale for the turbulence,  $u_{\text{turb}}$ , is the root mean square of the velocity fluctuation,  $\mathbf{u}'$ :

$$u_{\text{turb}} = \sqrt{\frac{u'_i u'_i}{3}}. \quad (\text{C3})$$

Under the assumptions that the turbulence is isotropic and  $l_o = (\sqrt{3/2} u_{\text{turb}})^3 / \epsilon$ , where  $\epsilon$  is an energy dissipation rate, a relation between  $\text{Re}_{l_o}$  and  $\text{Re}_{\lambda_T}$  can be obtained as [70]

$$\text{Re}_{\lambda_T} = \sqrt{\frac{20}{3}} \text{Re}_{l_o}. \quad (\text{C4})$$

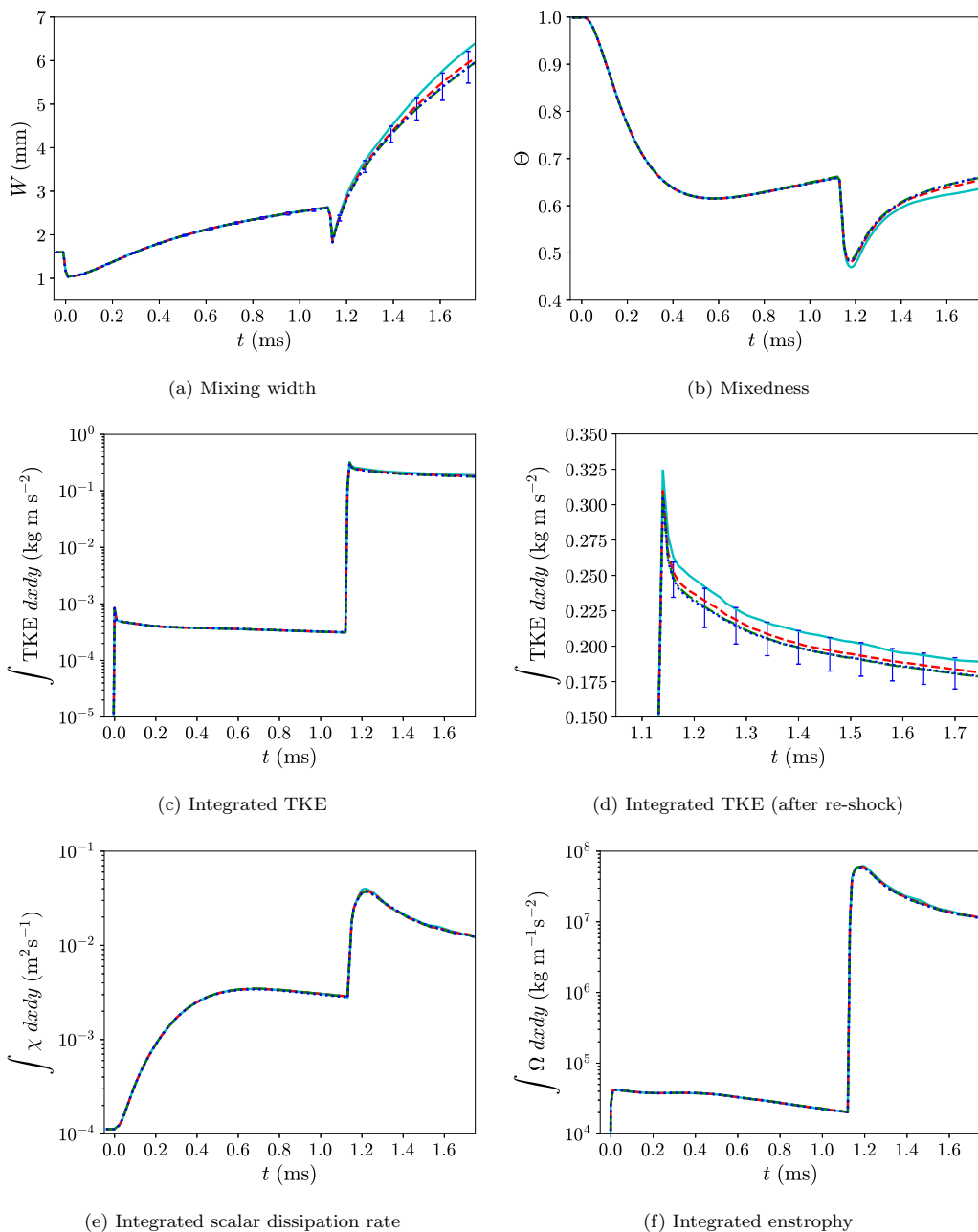


FIG. 28. Statistical sensitivities of different statistical quantities over time for the 2D problem with grid G. Cyan solid line, 6 realizations; red dashed line, 12 realizations; green dash-dotted line, 18 realizations; blue dotted line, 24 realizations. The error bars in some of the subfigures show the  $\pm$  one standard deviation of the corresponding quantities over 24 realizations.

Similar to Sec. VII, we approximate  $u_{\text{turb}} \approx u_{\text{rms}} = \sqrt{u'_i u'_i} / 3$ , since it can be seen from Sec. VIII G that switching  $\mathbf{u}'$  and  $\mathbf{u}''$  has unnoticeable effect on the energy contents. The length scale of the largest eddies is approximated by the mean of the integral length scales of velocity components



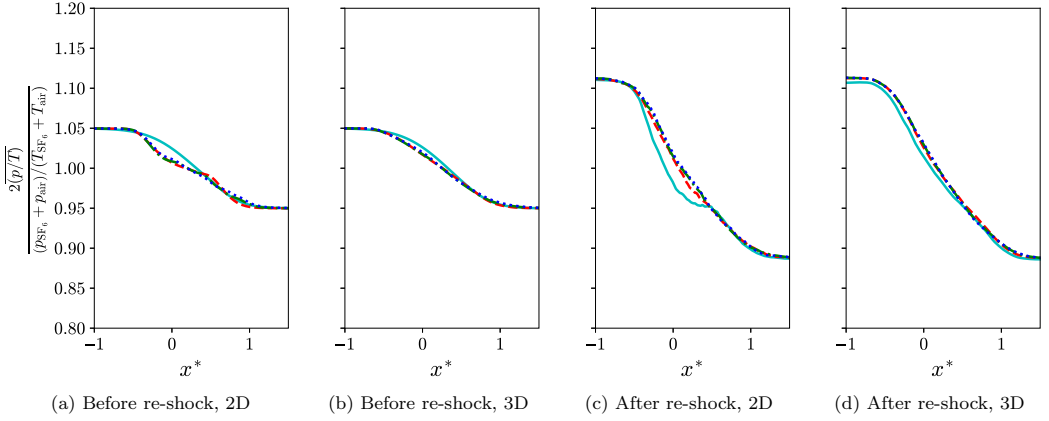


FIG. 29. Profiles of normalized ratio of pressure to temperature at different times for the 2D and 3D problems with physical transport coefficients. Before reshock:  $t^* = 0.9$  (cyan solid line);  $t^* = 7.5$  (red dashed line);  $t^* = 14.1$  (green dash-dotted line);  $t^* = 20.7$  (blue dotted line). After reshock:  $t^* = 22.6$  (cyan solid line);  $t^* = 26.3$  (red dashed line);  $t^* = 30.1$  (green dash-dotted line);  $t^* = 32.9$  (blue dotted line).

over the central part of the mixing layer. Therefore,  $\text{Re}_{l_o}$  and  $\text{Re}_{\lambda_T}$  within the central part of the mixing layer and  $\lambda_T$  can be estimated as

$$l_o \approx \frac{\langle l_u + l_v + l_w \rangle}{3}, \quad (\text{C5})$$

$$\langle \text{Re}_{l_o} \rangle \approx \sqrt{\frac{3}{2}} \left\langle \frac{\bar{\rho} u_{\text{rms}} l_o}{\bar{\mu}} \right\rangle, \quad (\text{C6})$$

$$\langle \text{Re}_{\lambda_T} \rangle \approx \sqrt{\frac{20}{3}} \langle \text{Re}_{l_o} \rangle, \quad (\text{C7})$$

$$\lambda_T \approx \left\langle \frac{\bar{\mu}}{\bar{\rho} u_{\text{rms}}} \right\rangle \langle \text{Re}_{\lambda_T} \rangle. \quad (\text{C8})$$

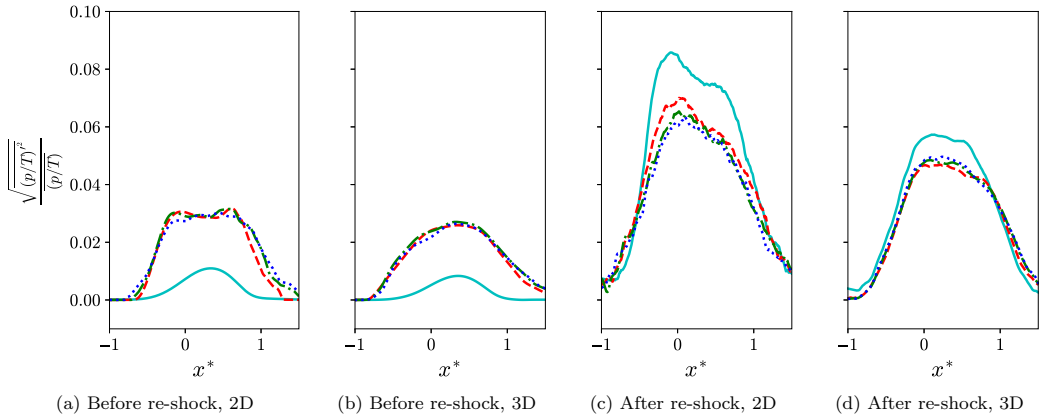


FIG. 30. Profiles of normalized standard deviation of ratio of pressure to temperature at different times for the 2D and 3D problems with physical transport coefficients. Before reshock:  $t^* = 0.9$  (cyan solid line);  $t^* = 7.5$  (red dashed line);  $t^* = 14.1$  (green dash-dotted line);  $t^* = 20.7$  (blue dotted line). After reshock:  $t^* = 22.6$  (cyan solid line);  $t^* = 26.3$  (red dashed line);  $t^* = 30.1$  (green dash-dotted line);  $t^* = 32.9$  (blue dotted line).

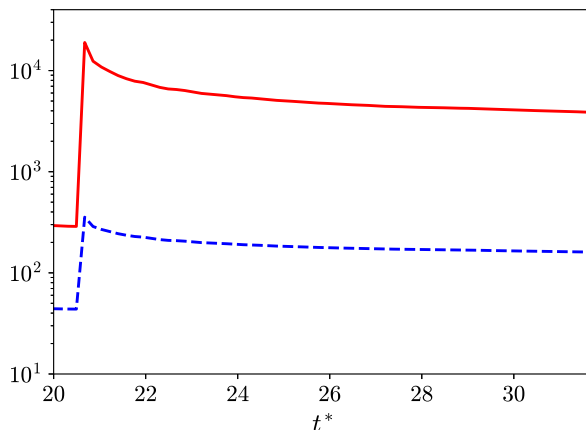


FIG. 31. Time evolution of the Reynolds numbers for the 3D problem with physical transport coefficients after reshock. Red solid line,  $\langle \text{Re}_{l_o} \rangle$ ; blue dashed line,  $\langle \text{Re}_{\lambda_T} \rangle$ .

The Kolmogorov microscale,  $\eta$ , which characterizes the smallest length scale in a turbulent flow, can be estimated as [70]

$$\frac{\eta}{l_o} \approx \langle \text{Re}_{l_o} \rangle^{-3/4}. \quad (\text{C9})$$

In the classical Kolmogorov theory [70,71], the emergence of the inertial range in spectral space requires that there is an intermediate scale,  $\lambda$ , which is not influenced by the outer-scale features and also eddies at the Kolmogorov microscale. In other words,  $\eta \ll \lambda \ll l_o$  is necessary. Dimotakis [72] proposed a more refined and stricter condition for mixing transition to occur if there exists an effective range of scales that is bounded by

$$\lambda_v \leq \lambda \leq \lambda_L, \quad (\text{C10})$$

where  $\lambda_L$  is the Liepmann-Taylor scale and  $\lambda_v$  is the inner viscous scale.  $\lambda_L$  is the smallest scale that can be generated directly by the outer scale  $l_o$  and  $\lambda_v$  is the the upper limit of the viscous range of the energy spectrum. Observed from experimental data, Dimotakis [72] suggested that  $\lambda_L$  is proportional to  $\lambda_T$ :

$$\lambda_L \approx c_L \lambda_T, \quad (\text{C11})$$

where  $c_L$  is a flow-dependent parameter. Following previous studies by Dimotakis [72], Zhou *et al.* [73], and Tritschler *et al.* [74], we use  $c_L = 5$ . Based on the experimental data on turbulent boundary layer flow by Saddoughi and Veeravalli [75] and results from RMI simulations by Tritschler *et al.* [74], it is reasonable to estimate  $\lambda_v$  as

$$\lambda_v \approx 50\eta. \quad (\text{C12})$$

Figure 31 shows the time evolution of  $\langle \text{Re}_{l_o} \rangle$  and  $\langle \text{Re}_{\lambda_T} \rangle$  for the highest Reynolds number 3D case (with physical transport coefficients) after reshock. Dimotakis [72] proposed that  $\langle \text{Re}_{l_o} \rangle \geq 10^4$  or  $\langle \text{Re}_{\lambda_T} \rangle \geq 100$  for mixing transition to occur. Although it is shown that  $\langle \text{Re}_{l_o} \rangle$  is only greater than  $10^4$  for a short duration after reshock,  $\langle \text{Re}_{\lambda_T} \rangle$  is greater than 100 throughout most of the simulation. This is an indication for mixing transition to occur in the corresponding 3D case. In Fig. 32, the comparison of the time evolution of different estimated length scales discussed earlier is shown for the time duration after reshock. It can be seen that  $\lambda_L$  is always greater than  $\lambda_v$  after reshock. This means an uncoupled range of scales exists and this is consistent with the observation of inertial range emergence from the scale decomposition of energy in Sec. VIII G. The coincidence of mixing transition with the appearance of the inertial range was also noted by Dimotakis [72].

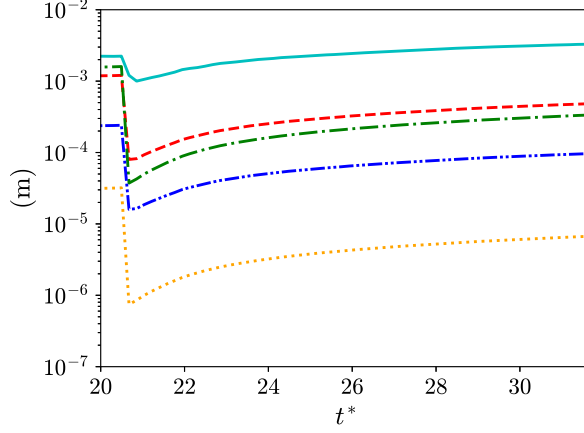


FIG. 32. Comparison of the length scales for the 3D problem with physical transport coefficients after reshock. Cyan solid line,  $l_o$ ; red dashed line,  $\lambda_L$ ; green dash-dotted line,  $\lambda_v$ ; blue dash-dot-dotted line,  $\lambda_T$ ; orange dotted line:  $\eta$ .

#### APPENDIX D: SPATIAL DISCRETIZATIONS

The Navier-Stokes equations given by Eqs. (1)–(3) can be rewritten in vector form. For example, the vector form for a 3D problem can be represented as

$$\frac{\partial \mathbf{Q}}{\partial t} + \frac{\partial \mathbf{F}}{\partial x} + \frac{\partial \mathbf{G}}{\partial y} + \frac{\partial \mathbf{H}}{\partial z} = -\frac{\partial \mathbf{F}_v}{\partial x} - \frac{\partial \mathbf{G}_v}{\partial y} - \frac{\partial \mathbf{H}_v}{\partial z}, \quad (\text{D1})$$

where  $\mathbf{Q}$  is the vectors of conservative variables.  $\mathbf{F}$ ,  $\mathbf{G}$ , and  $\mathbf{H}$  are the convective flux vectors in the  $x$ ,  $y$ , and  $z$  directions.  $\mathbf{F}_v$ ,  $\mathbf{G}_v$ , and  $\mathbf{H}_v$  are the diffusive or viscous flux vectors in the  $x$ ,  $y$ , and  $z$  directions.

The explicit form of a sixth-order weighted compact nonlinear scheme (WCNS) with nonlinear interpolation and approximate Riemann solver [37] is used to approximate the derivatives of the convective fluxes. The scheme is based on the sixth-order accurate explicit midpoint and node-to-node differencing (MND) by Nonomura and Fujii [76]. For example, the first derivative of the convective flux in the  $x$  direction,  $\mathbf{F}$ , at grid node  $(i, j, k)$  is approximated by  $\widehat{\partial \mathbf{F} / \partial x}|_{i,j,k}$  as

$$\begin{aligned} \frac{\partial \mathbf{F}}{\partial x} \Big|_{i,j,k} &\approx \widehat{\frac{\partial \mathbf{F}}{\partial x}} \Big|_{i,j,k} = \frac{1}{\Delta x} \left[ \frac{3}{2} (\tilde{\mathbf{F}}_{i+\frac{1}{2},j,k} - \tilde{\mathbf{F}}_{i-\frac{1}{2},j,k}) - \frac{3}{10} (\mathbf{F}_{i+1,j,k} - \mathbf{F}_{i-1,j,k}) \right. \\ &\quad \left. + \frac{1}{30} (\tilde{\mathbf{F}}_{i+\frac{3}{2},j,k} - \tilde{\mathbf{F}}_{i-\frac{3}{2},j,k}) \right], \end{aligned} \quad (\text{D2})$$

where  $\tilde{\mathbf{F}}_{i+\frac{1}{2},j,k}$  are fluxes approximated at midpoints between cell nodes by the sixth-order accurate nonlinear localized dissipation interpolation and hybrid Riemann solver given by Wong and Lele [37].  $\mathbf{F}_{i,j,k}$  are the fluxes at cell nodes and  $\Delta x$  is the uniform grid spacing in the  $x$  direction. Note that Eq. (D2) uses  $\mathbf{F}_{i-1,j,k}$  and  $\mathbf{F}_{i+1,j,k}$  instead of  $\tilde{\mathbf{F}}_{i-1,j,k}$  and  $\tilde{\mathbf{F}}_{i+1,j,k}$  since the fluxes at nodes can be directly evaluated from the conservative variables at nodes and require no interpolation. The MND scheme given by Eq. (D2) can be rewritten in flux-difference form, which is given by

$$\widehat{\frac{\partial \mathbf{F}}{\partial x}} \Big|_{i,j,k} = \frac{1}{\Delta x} (\hat{\mathbf{F}}_{i+\frac{1}{2},j,k} - \hat{\mathbf{F}}_{i-\frac{1}{2},j,k}), \quad (\text{D3})$$

where

$$\widehat{\mathbf{F}}_{i+\frac{1}{2},j,k} = \frac{1}{30}\tilde{\mathbf{F}}_{i-\frac{1}{2},j,k} - \frac{3}{10}\mathbf{F}_{i,j,k} + \frac{23}{15}\tilde{\mathbf{F}}_{i+\frac{1}{2},j,k} - \frac{3}{10}\mathbf{F}_{i+1,j,k} + \frac{1}{30}\tilde{\mathbf{F}}_{i+\frac{3}{2},j,k}. \quad (\text{D4})$$

Any central explicit or compact (implicit) finite difference scheme can be rewritten into the flux-difference form and it is derived in Ref. [77]. The MND scheme in flux-difference form is implemented in HAMeRS to ensure that the discretizations of the convective fluxes are conservative at the coarse-fine AMR grid boundaries with the patch-based AMR method by Berger and Colella [78]. Conservative linear spatial interpolation or prolongation is adopted for projecting solutions from coarse grids to fine grids in the simulations. Conservative averaging is also used to update coarse cells covered by finer cells. The conservative spatial discretizations ensure that shock waves are moving at the correct speeds. Note that explicit sixth-order finite differences are used to compute the derivatives of diffusive and viscous fluxes in nonconservative form but the effects on the shock waves are negligible compared to those from the discretizations of the convective fluxes as the shocks are not well resolved in the simulations.

## APPENDIX E: SENSORS FOR ADAPTIVE MESH REFINEMENT

Three different types of sensors were used in the AMR simulations to identify regions for refinement. They include the gradient sensor on pressure field, the multiresolution wavelet sensor on density field, and the value sensor on the mass fraction fields. In this section, the first two types of sensors are discussed.

### 1. Gradient sensor

The gradient sensor on pressure field,  $p$ , by Jameson *et al.* [79] is chosen to detect shock waves. The sensor for a 3D problem is given by

$$\begin{aligned} (w_x)_{i,j,k} &= |p_{i+1,j,k} - 2p_{i,j,k} + p_{i-1,j,k}|, \\ (w_y)_{i,j,k} &= |p_{i,j+1,k} - 2p_{i,j,k} + p_{i,j-1,k}|, \\ (w_z)_{i,j,k} &= |p_{i,j,k+1} - 2p_{i,j,k} + p_{i,j,k-1}|, \end{aligned} \quad (\text{E1})$$

$$\tilde{w}_{i,j,k} = \frac{\sqrt{\{(w_x)_{i,j,k}\}^2 + \{(w_y)_{i,j,k}\}^2 + \{(w_z)_{i,j,k}\}^2}}{\mathcal{M}_{(i,j,k) \in S}(p_{i,j,k}) + \epsilon},$$

where  $S$  is the combined stencil of the three second-order accurate central differences  $((w_x)_{i,j,k}$ ,  $(w_y)_{i,j,k}$ , and  $(w_z)_{i,j,k}$ ) and  $\epsilon$  is a small value to prevent division by zero. The local ‘‘mean’’,  $\mathcal{M}_{(i,j) \in S}(p_{i,j,k})$ , is defined as

$$\begin{aligned} \mathcal{M}_{(i,j,k) \in S}(p_{i,j,k}) &= \sqrt{(p_{i+1,j,k} + 2p_{i,j,k} + p_{i-1,j,k})^2 + (p_{i,j+1,k} + 2p_{i,j,k} + p_{i,j-1,k})^2} \\ &\quad + (p_{i,j,k+1} + 2p_{i,j,k} + p_{i,j,k-1})^2. \end{aligned} \quad (\text{E2})$$

Grid cells are tagged for refinement if  $\tilde{w}_{i,j,k}$  is greater than a tolerance. It should be noted that the normalized gradient sensor always has values between zero and one. A tolerance of 0.002 is chosen for the gradient sensor for all simulations in this paper.

### 2. Multiresolution wavelet sensor

A multiresolution wavelet sensor on the density field,  $\rho$ , is used to detect mixing and chaotic regions. In wavelet decomposition, the amount of features at location  $x = x_j$  having a characteristic length of  $2^m$  or at scale level  $m$  is measured through the wavelet coefficient  $w_j^{(m)}$ . The wavelet

coefficients in 1D space are evaluated from the inner product of a quantity of interest ( $\rho$  is used here) with some wavelet functions  $\psi_j^{(m)}$ :

$$w_j^{(m)} = \langle \rho, \psi_j^{(m)} \rangle = \int_{-\infty}^{\infty} \rho(x) \psi_j^{(m)}(x) dx, \quad \forall m \in \{1, 2, \dots, m_{\max}\}, \quad (\text{E3})$$

where  $m_{\max}$  is the largest scale level chosen by user. In order to obtain the wavelet coefficients at different scale levels at each grid point, we follow Sjögreen and Yee [80] to use the redundant wavelets. The wavelet function at scale level  $m$  and location  $x = x_j$  is defined as

$$\psi_j^{(m)}(x) = \frac{1}{2^m} \psi\left(\frac{x - x_j}{2^m}\right), \quad (\text{E4})$$

where  $\psi(x)$  is the mother wavelet. The Harten wavelet modified by Sjögreen and Yee [80] is used and the wavelet coefficients can be computed by

$$w_j^{(m)} = -\frac{1}{2}(\rho_{j+2^{m-1}}^{(m-1)} - 2\rho_j^{(m-1)} + \rho_{j-2^{m-1}}^{(m-1)}), \quad (\text{E5})$$

$$\rho_j^{(m)} = \frac{1}{2}(\rho_{j+2^{m-1}}^{(m-1)} + \rho_{j-2^{m-1}}^{(m-1)}), \quad (\text{E6})$$

where  $\rho_j^{(m)}$  is the scaling coefficient at the same scale level and location as the wavelet coefficient,  $w_j^{(m)}$ . The wavelet and scaling coefficients at different levels and locations can be computed recursively from lower levels, where  $\rho_j^{(0)} = \rho_j$  at the lowest level.

Wavelet coefficients in a 3D space are estimated from the 1D wavelet coefficients in different directions. The 1D wavelet coefficients in a 3D space are given by

$$(w_x)_{i,j,k}^{(m)} = \int_{-\infty}^{\infty} \rho(x, y, z) \psi_i^{(m)}(x) dx, \quad (\text{E7})$$

$$(w_y)_{i,j,k}^{(m)} = \int_{-\infty}^{\infty} \rho(x, y, z) \psi_j^{(m)}(y) dy, \quad (\text{E8})$$

$$(w_z)_{i,j,k}^{(m)} = \int_{-\infty}^{\infty} \rho(x, y, z) \psi_k^{(m)}(z) dz. \quad (\text{E9})$$

The 3D wavelet coefficients are then estimated from the 1D wavelet coefficients:

$$w_{i,j,k}^{(m)} = \sqrt{\{(w_x)_{i,j,k}^{(m)}\}^2 + \{(w_y)_{i,j,k}^{(m)}\}^2 + \{(w_z)_{i,j,k}^{(m)}\}^2}. \quad (\text{E10})$$

We define the wavelet sensors as the wavelet coefficients normalized by the local ‘‘mean’’ of the scaling coefficients at one lower level:

$$\tilde{w}_{i,j,k}^{(m)} = \frac{w_{i,j,k}^{(m)}}{\mathcal{M}_{(i,j,k) \in S}(\rho_{i,j,k}^{(m-1)}) + \epsilon}. \quad (\text{E11})$$

The local ‘‘mean’’ of the scaling coefficients of Harten wavelet,  $\mathcal{M}_{(i,j,k) \in S}(\rho_{i,j,k}^{(m-1)})$ , is defined as

$$\begin{aligned} \mathcal{M}_{(i,j,k) \in S}(\rho_{i,j,k}^{(m-1)}) &= \frac{1}{2} [\{\rho_{i+2^{m-1},j,k}^{(m-1)} + 2\rho_{i,j,k}^{(m-1)} + \rho_{i-2^{m-1},j,k}^{(m-1)}\}^2 + \{\rho_{i,j+2^{m-1},k}^{(m-1)} + 2\rho_{i,j,k}^{(m-1)} + \rho_{i,j-2^{m-1},k}^{(m-1)}\}^2 \\ &\quad + \{\rho_{i,j,k+2^{m-1}}^{(m-1)} + 2\rho_{i,j,k}^{(m-1)} + \rho_{i,j,k-2^{m-1}}^{(m-1)}\}^2]^{\frac{1}{2}}. \end{aligned} \quad (\text{E12})$$

If  $\tilde{w}_{i,j}^{(m)}$  at any scale level is greater than a user-defined tolerance, the corresponding grid cell is tagged for refinement. It should be noted that the local ‘‘mean’’ is designed in a way that the sensor

TABLE V. Fluid properties.

Gas	$\gamma_i$	$c_{p,i}$ (J kg <sup>-1</sup> K <sup>-1</sup> )	$c_{v,i}$ (J kg <sup>-1</sup> K <sup>-1</sup> )	$M_i$ (g mol <sup>-1</sup> )	$R_i$ (J kg <sup>-1</sup> K <sup>-1</sup> )	$(\epsilon/k)_i$ (K)	$\sigma_i$ (Å)	$Pr_i$
SF <sub>6</sub>	1.09312	668.286	611.359	146.055	56.9269	222.1	5.128	0.79
Air	1.39909	1040.50	743.697	28.0135	296.802	78.6	3.711	0.71

applied to the finest level of scale is the gradient sensor discussed in previous section.  $m_{\max} = 3$  and a tolerance of 0.004 for all wavelet sensors are chosen for all simulations in this paper.

### APPENDIX F: TRANSPORT COEFFICIENTS

The shear viscosity,  $\mu_i$ , of a species  $i$  is given by the Chapman-Enskog's model [81]:

$$\mu_i = 2.6693 \times 10^{-6} \frac{\sqrt{M_i T}}{\Omega_{\mu,i} \sigma_i^2}, \quad (\text{F1})$$

where  $\sigma_i$  is the collision diameter and  $\Omega_{\mu,i}$  is the collision integral of the species given by

$$\Omega_{\mu,i} = A(T_i^*)^B + C \exp(DT_i^*) + E \exp(FT_i^*), \quad (\text{F2})$$

where  $T_i^* = T/(\epsilon/k)_i$ ,  $A = 1.16145$ ,  $B = -0.14874$ ,  $C = 0.52487$ ,  $D = -0.7732$ ,  $E = 2.16178$ , and  $F = -2.43787$ .  $T$  is the temperature of the species.  $(\epsilon/k)_i$  is the Lennard-Jones energy parameter and  $M_i$  is the molecular weight of the species. The values of  $M_i$ ,  $(\epsilon/k)_i$ , and  $\sigma_i$  of different species are given in Table V.

The bulk viscosity,  $\mu_v$ , of air is given by the linear model by Gu and Ubachs [82],

$$\mu_v = A + BT, \quad (\text{F3})$$

where  $A = -3.15 \times 10^{-5}$  kg m<sup>-1</sup> s<sup>-1</sup> and  $B = 1.58 \times 10^{-7}$  kg m<sup>-1</sup> s<sup>-1</sup> K<sup>-1</sup>.

The bulk viscosity,  $\mu_v$ , of SF<sub>6</sub> is given by the Cramer's model [83]:

$$\mu_v = (\gamma - 1)^2 c_v|_v (p\tau_v), \quad (\text{F4})$$

$$c_v|_v = \left( \frac{c_v}{R} - \frac{f_r + 3}{2} \right), \quad (\text{F5})$$

$$(p\tau_v) = A \exp\left( \frac{B}{T^{1/3}} + \frac{C}{T^{2/3}} \right), \quad (\text{F6})$$

where  $f_r = 3$ ,  $A = 0.2064 \times 10^{-5}$  kg m<sup>-1</sup> s<sup>-1</sup>,  $B = 121$  K<sup>1/3</sup>, and  $C = -339$  K<sup>2/3</sup> for SF<sub>6</sub>.

The thermal conductivity of species  $i$ ,  $\kappa_i$ , is defined by

$$\kappa_i = c_{p,i} \frac{\mu_i}{Pr_i}, \quad (\text{F7})$$

where  $Pr_i$  and  $c_{p,i}$  are the species-specific Prandtl number and specific heat at constant pressure respectively.

Mass diffusion coefficient of a binary mixture,  $D_{ij}$ , is given by [84]

$$D_{ij} = D_i = D_j = \frac{0.0266}{\Omega_{D,ij}} \frac{T^{3/2}}{p \sqrt{M_{ij} \sigma_{ij}^2}}, \quad (\text{F8})$$

where  $p$  and  $T$  are the pressure and temperature of the mixture.  $\Omega_{D,ij}$  is the collision integral for diffusion given by

$$\Omega_{D,ij} = A(T_{ij}^*)^B + C \exp(DT_{ij}^*) + E \exp(FT_{ij}^*) + G \exp(HT_{ij}^*), \quad (\text{F9})$$

where  $T_{ij}^* = T/T_{\epsilon_{ij}}$ ,  $A = 1.06036$ ,  $B = -0.1561$ ,  $C = 0.19300$ ,  $D = -0.47635$ ,  $E = 1.03587$ ,  $F = -1.52996$ ,  $G = 1.76474$ , and  $H = -3.89411$ .  $M_{ij}$ ,  $\sigma_{ij}$ , and  $T_{\epsilon_{ij}}$  are the effective molecular weight, collision diameter, and Lennard-Jones energy parameter respectively for the mixture:

$$M_{ij} = \frac{2}{\frac{1}{M_i} + \frac{1}{M_j}}, \quad (\text{F10})$$

$$\sigma_{ij} = \frac{\sigma_i + \sigma_j}{2}, \quad (\text{F11})$$

$$T_{\epsilon_{ij}} = \sqrt{\left(\frac{\epsilon}{k}\right)_i \left(\frac{\epsilon}{k}\right)_j}. \quad (\text{F12})$$

The values of  $M_i$ ,  $(\epsilon/k)_i$ , and  $\sigma_i$  of different species are given in Table V.

### APPENDIX G: MIXING RULES

With the assumption that all species are at pressure and temperature equilibria, the ratio of specific heats of the mixture follows as

$$\gamma = \frac{c_p}{c_v}, \quad c_p = \sum_{i=1}^N Y_i c_{p,i}, \quad c_v = \sum_{i=1}^N Y_i c_{v,i}. \quad (\text{G1})$$

The molecular weight of the mixture is given by

$$M = \left( \sum_{i=1}^N \frac{Y_i}{M_i} \right)^{-1}. \quad (\text{G2})$$

The mixture shear viscosity, bulk viscosity, and thermal conductivity are given by

$$\mu = \frac{\sum_{i=1}^N \mu_i Y_i / \sqrt{M_i}}{\sum_{i=1}^N Y_i / \sqrt{M_i}}, \quad (\text{G3})$$

$$\mu_v = \frac{\sum_{i=1}^N \mu_{v,i} Y_i / \sqrt{M_i}}{\sum_{i=1}^N Y_i / \sqrt{M_i}}, \quad (\text{G4})$$

$$\kappa = \frac{\sum_{i=1}^N \kappa_i Y_i / \sqrt{M_i}}{\sum_{i=1}^N Y_i / \sqrt{M_i}}. \quad (\text{G5})$$

- 
- [1] R. D. Richtmyer, Taylor instability in shock acceleration of compressible fluids, *Commun. Pure Appl. Math.* **13**, 297 (1960).
  - [2] E. E. Meshkov, Instability of the interface of two gases accelerated by a shock wave, *Fluid Dyn.* **4**, 101 (1969).
  - [3] M. Brouillette, The Richtmyer-Meshkov instability, *Annu. Rev. Fluid Mech.* **34**, 445 (2002).
  - [4] Y. Zhou, Rayleigh-Taylor and Richtmyer-Meshkov instability induced flow, turbulence, and mixing. I, *Phys. Rep.* **720**, 1 (2017).
  - [5] Y. Zhou, Rayleigh-Taylor and Richtmyer-Meshkov instability induced flow, turbulence, and mixing. II, *Phys. Rep.* **723**, 1 (2017).
  - [6] B. Thornber, D. Drikakis, D. L. Youngs, and R. J. R. Williams, The influence of initial conditions on turbulent mixing due to Richtmyer-Meshkov instability, *J. Fluid Mech.* **654**, 99 (2010).
  - [7] O. Schilling and M. Latini, High-order WENO simulations of three-dimensional reshocked Richtmyer-Meshkov instability to late times: Dynamics, dependence on initial conditions, and comparisons to experimental data, *Acta Math. Sci* **30**, 595 (2010).
  - [8] B. Thornber, D. Drikakis, D. L. Youngs, and R. J. R. Williams, Growth of a Richtmyer-Meshkov turbulent layer after reshock, *Phys. Fluids* **23**, 095107 (2011).

- [9] M. Hahn, D. Drikakis, D. L. Youngs, and R. J. R. Williams, Richtmyer-Meshkov turbulent mixing arising from an inclined material interface with realistic surface perturbations and reshocked flow, *Phys. Fluids* **23**, 046101 (2011).
- [10] F. F. Grinstein, A. A. Gowardhan, and A. J. Wachtor, Simulations of Richtmyer-Meshkov instabilities in planar shock-tube experiments, *Phys. Fluids* **23**, 034106 (2011).
- [11] A. A. Gowardhan and F. F. Grinstein, Numerical simulation of Richtmyer-Meshkov instabilities in shocked gas curtains, *J. Turbulence* **12**, N43 (2011).
- [12] A. A. Gowardhan, J. R. Ristorcelli, and F. F. Grinstein, The bipolar behavior of the Richtmyer-Meshkov instability, *Phys. Fluids* **23**, 071701 (2011).
- [13] S. Balasubramanian, G. C. Orlicz, K. P. Prestridge, and B. J. Balakumar, Experimental study of initial condition dependence on Richtmyer-Meshkov instability in the presence of reshock, *Phys. Fluids* **24**, 034103 (2012).
- [14] B. J. Balakumar, G. C. Orlicz, J. R. Ristorcelli, S. Balasubramanian, K. P. Prestridge, and C. D. Tomkins, Turbulent mixing in a Richtmyer-Meshkov fluid layer after reshock: Velocity and density statistics, *J. Fluid Mech.* **696**, 67 (2012).
- [15] G. C. Orlicz, S. Balasubramanian, P. Vorobieff, and K. P. Prestridge, Mixing transition in a shocked variable-density flow, *Phys. Fluids* **27**, 114102 (2015).
- [16] M. Mohaghar, J. Carter, B. Musci, D. Reilly, J. McFarland, and D. Ranjan, Evaluation of turbulent mixing transition in a shock-driven variable-density flow, *J. Fluid Mech.* **831**, 779 (2017).
- [17] D. T. Reese, A. M. Ames, C. D. Noble, J. G. Oakley, D. A. Rothamer, and R. Bonazza, Simultaneous direct measurements of concentration and velocity in the Richtmyer-Meshkov instability, *J. Fluid Mech.* **849**, 541 (2018).
- [18] D. J. Hill, C. Pantano, and D. I. Pullin, Large-eddy simulation and multiscale modelling of a Richtmyer-Meshkov instability with reshock, *J. Fluid Mech.* **557**, 29 (2006).
- [19] M. Lombardini, D. J. Hill, D. I. Pullin, and D. I. Meiron, Atwood ratio dependence of Richtmyer-Meshkov flows under reshock conditions using large-eddy simulations, *J. Fluid Mech.* **670**, 439 (2011).
- [20] M. Lombardini, D. I. Pullin, and D. I. Meiron, Transition to turbulence in shock-driven mixing: A Mach number study, *J. Fluid Mech.* **690**, 203 (2012).
- [21] V. K. Tritschler, B. J. Olson, S. K. Lele, S. Hickel, X. Y. Hu, and N. A. Adams, On the Richtmyer-Meshkov instability evolving from a deterministic multimode planar interface, *J. Fluid Mech.* **755**, 429 (2014).
- [22] A. Subramaniam and S. K. Lele, Turbulence energetics in an inclined interface Richtmyer-Meshkov instability, in *10th International Symposium on Turbulence and Shear Flow Phenomena* (International Symposium on Turbulence and Shear Flow Phenomena, Chicago, IL, USA, 2017).
- [23] M. Lombardini, D. I. Pullin, and D. I. Meiron, Turbulent mixing driven by spherical implosions. Part 1. Flow description and mixing-layer growth, *J. Fluid Mech.* **748**, 85 (2014).
- [24] M. Lombardini, D. I. Pullin, and D. I. Meiron, Turbulent mixing driven by spherical implosions. Part 2. Turbulence statistics, *J. Fluid Mech.* **748**, 113 (2014).
- [25] B. J. Olson and J. A. Greenough, Comparison of two- and three-dimensional simulations of miscible Richtmyer-Meshkov instability with multimode initial conditions, *Phys. Fluids* **26**, 101702 (2014).
- [26] B. Thornber and Y. Zhou, Numerical simulations of the two-dimensional multimode Richtmyer-Meshkov instability, *Phys. Plasmas* **22**, 032309 (2015).
- [27] F. F. Grinstein, L. G. Margolin, and W. J. Rider, *Implicit Large Eddy Simulation: Computing Turbulent Fluid Dynamics* (Cambridge University Press, Cambridge, UK, 2007).
- [28] E. Garnier, N. Adams, and P. Sagaut, *Large Eddy Simulation for Compressible Flows* (Springer Science & Business Media, Berlin, 2009).
- [29] J. O. Hirschfelder, C. F. Curtiss, and R. B. Bird, *Molecular theory of gases and liquids*, Vol. 26 (Wiley, New York, 1954).
- [30] D. Livescu, Numerical simulations of two-fluid turbulent mixing at large density ratios and applications to the Rayleigh-Taylor instability, *Philos. Trans. R. Soc. A* **371**, 20120185 (2013).
- [31] F. A. Williams, *Combustion Theory* (CRC Press, Boca Raton, FL, 2018).
- [32] B. T. N. Gunney and R. W. Anderson, Advances in patch-based adaptive mesh refinement scalability, *J. Parallel Distributed Comput.* **89**, 65 (2016).



- [33] B. T. N. Gunney, A. M. Wissink, and D. A. Hysom, Parallel clustering algorithms for structured AMR, *J. Parallel Distributed Comput.* **66**, 1419 (2006).
- [34] R. D. Hornung, A. M. Wissink, and S. R. Kohn, Managing complex data and geometry in parallel structured AMR applications, *Eng. Comput.* **22**, 181 (2006).
- [35] R. D. Hornung and S. R. Kohn, Managing application complexity in the SAMRAI object-oriented framework, *Concurrency Comput. Pract. Exper.* **14**, 347 (2002).
- [36] A. M. Wissink, R. D. Hornung, S. R. Kohn, S. S. Smith, and N. Elliott, Large scale parallel structured AMR calculations using the SAMRAI framework, in *Supercomputing, ACM/IEEE 2001 Conference* (IEEE, Denver, CO, USA, 2001), pp. 22–22.
- [37] M. L. Wong and S. K. Lele, High-order localized dissipation weighted compact nonlinear scheme for shock-and interface-capturing in compressible flows, *J. Comput. Phys.* **339**, 179 (2017).
- [38] C.-W. Shu and S. Osher, Efficient implementation of essentially non-oscillatory shock-capturing schemes, II, *J. Comput. Phys.* **83**, 32 (1989).
- [39] M. L. Wong and S. K. Lele, Multiresolution feature detection in adaptive mesh refinement with high-order shock-and interface-capturing scheme, in *46th AIAA Fluid Dynamics Conference, AIAA Aviation* (AIAA, Washington, D.C., USA, 2016).
- [40] M. Vetter and B. Sturtevant, Experiments on the Richtmyer-Meshkov instability of an air/SF<sub>6</sub> interface, *Shock Waves* **4**, 247 (1995).
- [41] F. Poggi, M.-H. Thorembey, and G. Rodriguez, Velocity measurements in turbulent gaseous mixtures induced by Richtmyer-Meshkov instability, *Phys. Fluids* **10**, 2698 (1998).
- [42] J. K. Prasad, A. Rasheed, S. Kumar, and B. Sturtevant, The late-time development of the Richtmyer-Meshkov instability, *Phys. Fluids* **12**, 2108 (2000).
- [43] R. E. Duff, F. H. Harlow, and C. W. Hirt, Effects of diffusion on interface instability between gases, *Phys. Fluids* **5**, 417 (1962).
- [44] M. Brouillette and B. Sturtevant, Experiments on the Richtmyer-Meshkov instability: Single-scale perturbations on a continuous interface, *J. Fluid Mech.* **263**, 271 (1994).
- [45] C. R. Weber, A. W. Cook, and R. Bonazza, Growth rate of a shocked mixing layer with known initial perturbations, *J. Fluid Mech.* **725**, 372 (2013).
- [46] D. L. Youngs, Numerical simulation of mixing by Rayleigh-Taylor and Richtmyer-Meshkov instabilities, *Laser Part. Beams* **12**, 725 (1994).
- [47] G. V. Candler and P. Dimotakis, Baroclinic torque and implications for subgrid-scale modeling, in *7th AIAA theoretical fluid mechanics conference* (AIAA, Atlanta, USA, 2014), p. 3214.
- [48] G. S. Sidharth and G. V. Candler, Subgrid-scale effects in compressible variable-density decaying turbulence, *J. Fluid Mech.* **846**, 428 (2018).
- [49] A. W. Cook, W. Cabot, and P. L. Miller, The mixing transition in Rayleigh-Taylor instability, *J. Fluid Mech.* **511**, 333 (2004).
- [50] D. Livescu, J. R. Ristorcelli, R. A. Gore, S. H. Dean, W. H. Cabot, and A. W. Cook, High Reynolds number Rayleigh-Taylor turbulence, *J. Turbulence* **10**, N13 (2009).
- [51] D. Livescu, J. R. Ristorcelli, M. R. Petersen, and R. A. Gore, New phenomena in variable-density Rayleigh-Taylor turbulence, *Phys. Scr.* **T142**, 014015 (2010).
- [52] G. Dimonte, C. E. Frerking, and M. Schneider, Richtmyer-Meshkov Instability in the Turbulent Regime, *Phys. Rev. Lett.* **74**, 4855 (1995).
- [53] G. Dimonte and M. Schneider, Density ratio dependence of Rayleigh-Taylor mixing for sustained and impulsive acceleration histories, *Phys. Fluids* **12**, 304 (2000).
- [54] Y. Zhou, A scaling analysis of turbulent flows driven by Rayleigh-Taylor and Richtmyer-Meshkov instabilities, *Phys. Fluids* **13**, 538 (2001).
- [55] B. Thornber, J. Griffond, O. Poujade, N. Attal, H. Varshochi, P. Bigdelou, P. Ramaprabhu, B. Olson, J. Greenough, Y. Zhou *et al.*, Late-time growth rate, mixing, and anisotropy in the multimode narrowband Richtmyer-Meshkov instability: The  $\theta$ -group collaboration, *Phys. Fluids* **29**, 105107 (2017).
- [56] D. Livescu and J. R. Ristorcelli, Variable-density mixing in buoyancy-driven turbulence, *J. Fluid Mech.* **605**, 145 (2008).

- [57] Y. Tian, F. Jaber, Z. Li, and D. Livescu, Numerical study of variable density turbulence interaction with a normal shock wave, *J. Fluid Mech.* **829**, 551 (2017).
- [58] P. Movahed and E. Johnsen, The mixing region in freely decaying variable-density turbulence, *J. Fluid Mech.* **772**, 386 (2015).
- [59] S. Gerashchenko and K. Prestridge, Density and velocity statistics in variable density turbulent mixing, *J. Turbulence* **16**, 1011 (2015).
- [60] B. Thornber, Impact of domain size and statistical errors in simulations of homogeneous decaying turbulence and the Richtmyer-Meshkov instability, *Phys. Fluids* **28**, 045106 (2016).
- [61] G. K. Batchelor and I. Proudman, The large-scale structure of homogenous turbulence, *Philos. Trans. R. Soc. London A* **248**, 369 (1956).
- [62] P. G. Saffman, Note on decay of homogeneous turbulence, *Phys. Fluids* **10**, 1349 (1967).
- [63] P. G. Saffman, The large-scale structure of homogeneous turbulence, *J. Fluid Mech.* **27**, 581 (1967).
- [64] D. Livescu, F. A. Jaber, and C. K. Madnia, The effects of heat release on the energy exchange in reacting turbulent shear flow, *J. Fluid Mech.* **450**, 35 (2002).
- [65] C. R. Weber, N. S. Haehn, J. G. Oakley, D. A. Rothamer, and R. Bonazza, An experimental investigation of the turbulent mixing transition in the Richtmyer-Meshkov instability, *J. Fluid Mech.* **748**, 457 (2014).
- [66] A. W. Cook and Y. Zhou, Energy transfer in Rayleigh-Taylor instability, *Phys. Rev. E* **66**, 026312 (2002).
- [67] C. A. Z. Towery, A. Y. Poludnenko, J. Urzay, J. O'Brien, M. Ihme, and P. E. Hamlington, Spectral kinetic energy transfer in turbulent premixed reacting flows, *Phys. Rev. E* **93**, 053115 (2016).
- [68] P. Grete, B. W. O'Shea, K. Beckwith, W. Schmidt, and A. Christlieb, Energy transfer in compressible magnetohydrodynamic turbulence, *Phys. Plasmas* **24**, 092311 (2017).
- [69] D. Zhao and H. Aluie, Inviscid criterion for decomposing scales, *Phys. Rev. Fluids* **3**, 054603 (2018).
- [70] S. B. Pope, *Turbulent Flows* (Cambridge University Press, Cambridge, UK, 2000).
- [71] G. K. Batchelor, *The Theory of Homogeneous Turbulence* (Cambridge University Press, Cambridge, UK, 1953).
- [72] P. E. Dimotakis, The mixing transition in turbulent flows, *J. Fluid Mech.* **409**, 69 (2000).
- [73] Y. Zhou, H. F. Robey, and A. C. Buckingham, Onset of turbulence in accelerated high-Reynolds-number flow, *Phys. Rev. E* **67**, 056305 (2003).
- [74] V. K. Tritschler, M. Zobel, S. Hickel, and N. A. Adams, Evolution of length scales and statistics of Richtmyer-Meshkov instability from direct numerical simulations, *Phys. Rev. E* **90**, 063001 (2014).
- [75] S. G. Saddoughi and S. V. Veeravalli, Local isotropy in turbulent boundary layers at high Reynolds number, *J. Fluid Mech.* **268**, 333 (1994).
- [76] T. Nonomura and K. Fujii, Robust explicit formulation of weighted compact nonlinear scheme, *Comput. Fluids* **85**, 8 (2013).
- [77] A. Subramaniam, M. L. Wong, and S. K. Lele, A high-order weighted compact high resolution scheme with boundary closures for compressible turbulent flows with shocks, *J. Comput. Phys.* **397**, 108822 (2019).
- [78] M. J. Berger and P. Colella, Local adaptive mesh refinement for shock hydrodynamics, *J. Comput. Phys.* **82**, 64 (1989).
- [79] A. Jameson, W. Schmidt, and E. Turkel, Numerical solutions of the Euler equations by finite volume methods using Runge Kutta time stepping schemes, in *14th Fluid and Plasma Dynamics Conference*, Vol. 1259 (AIAA, Palo Alto, CA, USA, 1981).
- [80] B. Sjögren and H. C. Yee, Multiresolution wavelet based adaptive numerical dissipation control for high order methods, *J. Sci. Comput.* **20**, 211 (2004).
- [81] S. Chapman and T. G. Cowling, The mathematical theory of non-uniform gases, in *The Mathematical Theory of Non-uniform Gases*, edited by S. Chapman and T. G. Cowling (Cambridge University Press, Cambridge, UK, 1991), p. 447.
- [82] Z. Gu and W. Ubachs, A systematic study of Rayleigh-Brillouin scattering in air, N<sub>2</sub>, and O<sub>2</sub> gases, *J. Chem. Phys.* **141**, 104320 (2014).
- [83] M. S. Cramer, Numerical estimates for the bulk viscosity of ideal gases, *Phys. Fluids* **24**, 066102 (2012).
- [84] B. E. Poling, J. M. Prausnitz, J. P. O'Connell, and R. C. Reid, *The Properties of Gases and Liquids* (McGraw-Hill, New York, 2001), Vol. 5.